

# Disease-related mutations in PI3K $\gamma$ disrupt regulatory C-terminal dynamics and reveal a path to selective inhibitors

Manoj K Rathinaswamy<sup>1</sup>, Zied Gaieb<sup>2†</sup>, Kaelin D Fleming<sup>1†</sup>, Chiara Borsari<sup>3</sup>, Noah J Harris<sup>1</sup>, Brandon E Moeller<sup>1</sup>, Matthias P Wymann<sup>3</sup>, Rommie E Amaro<sup>2</sup>, John E Burke<sup>1,4\*</sup>

<sup>1</sup>Department of Biochemistry and Microbiology, University of Victoria, Victoria, Canada; <sup>2</sup>Department of Chemistry and Biochemistry, University of California San Diego, San Diego, United States; <sup>3</sup>University of Basel, Department of Biomedicine, Basel, Switzerland; <sup>4</sup>Department of Biochemistry and Molecular Biology, The University of British Columbia, Vancouver, Canada

**Abstract** Class I Phosphoinositide 3-kinases (PI3Ks) are master regulators of cellular functions, with the class IB PI3K catalytic subunit (p110 $\gamma$ ) playing key roles in immune signalling. p110 $\gamma$  is a key factor in inflammatory diseases and has been identified as a therapeutic target for cancers due to its immunomodulatory role. Using a combined biochemical/biophysical approach, we have revealed insight into regulation of kinase activity, specifically defining how immunodeficiency and oncogenic mutations of R1021 in the C-terminus can inactivate or activate enzyme activity. Screening of inhibitors using HDX-MS revealed that activation loop-binding inhibitors induce allosteric conformational changes that mimic those in the R1021C mutant. Structural analysis of advanced PI3K inhibitors in clinical development revealed novel binding pockets that can be exploited for further therapeutic development. Overall, this work provides unique insights into regulatory mechanisms that control PI3K $\gamma$  kinase activity and shows a framework for the design of PI3K isoform and mutant selective inhibitors.

\*For correspondence:  
jeburke@uvic.ca

†These authors contributed  
equally to this work

**Competing interests:** The  
authors declare that no  
competing interests exist.

**Funding:** See page 21

**Received:** 08 November 2020

**Accepted:** 03 March 2021

**Published:** 04 March 2021

**Reviewing editor:** Amy  
Andreotti, Iowa State University,  
United States

© Copyright Rathinaswamy et al.  
This article is distributed under  
the terms of the [Creative  
Commons Attribution License](#),  
which permits unrestricted use  
and redistribution provided that  
the original author and source are  
credited.

## Introduction

The phosphoinositide 3-kinase (PI3K) family of enzymes are central regulators of growth, proliferation, migration, and metabolism in a plethora of cells and tissues (*Bilanges et al., 2019; Madsen and Vanhaesebroeck, 2020*). PI3Ks are lipid kinases that generate the lipid second messenger phosphatidylinositol-3,4,5-trisphosphate (PIP<sub>3</sub>), which is utilised downstream of cell surface receptors to regulate growth, metabolism, survival, and differentiation (*Bilanges et al., 2019*). PIP<sub>3</sub> is generated by four distinct class I PI3K catalytic isoforms separated into two groups: class IA (p110 $\alpha$ , p110 $\beta$ , and p110 $\delta$ ) and class IB (p110 $\gamma$ ). All class I PI3Ks are constitutively associated with regulatory subunits, and the primary difference between class IA and class IB PI3Ks is their association with unique regulatory subunits. Class IA PI3Ks bind p85-like regulatory subunits encoded by *PIK3R1*, *PIK3R2*, *PIK3R3*, and class IB PI3K bind either a p101 or a p84 (also called p87<sup>PIKAP</sup>) regulatory subunit (*Suire et al., 2005; Stephens et al., 1997; Bohnacker et al., 2009*). The four catalytic subunits of class I PI3K isoforms have distinct expression profiles: p110 $\alpha$  and p110 $\beta$  are ubiquitously expressed, and p110 $\delta$  and p110 $\gamma$  are mainly localised in immune cells (*Bilanges et al., 2019*). All PI3K isoforms have been implicated in a variety of human diseases, including cancer, immunodeficiencies, inflammation, and developmental disorders (*Goncalves et al., 2018; Fruman et al., 2017; Burke, 2018*).

The class IB p110 $\gamma$  isoform encoded by *PIK3CG* is a master regulator of immune cell function. It carries out almost all its physiological functions in the cell when bound to regulatory subunits, with these complexes frequently referred to as PI3K $\gamma$  (which can be either p110 $\gamma$ /p101 or p110 $\gamma$ /p84). PI3K $\gamma$  plays important roles in the regulation of myeloid (macrophages, mast cells, neutrophils) and lymphoid (T cells, B cells, and Natural Killer cells) -derived immune cells (Camps et al., 2005; Patrucco et al., 2004; Hirsch et al., 2000). It regulates immune cell chemotaxis (Hirsch et al., 2000; Li et al., 2000; Sasaki et al., 2000a), cytokine release (Laffargue et al., 2002; Collmann et al., 2013), and generation of reactive oxygen species (Hirsch et al., 2000), which are important processes in both the innate and adaptive immune systems. The ability of PI3K $\gamma$  to mediate multiple immune cell functions is controlled by its activation downstream of numerous cell surface receptors, including G-protein coupled receptors (GPCRs) (Stoyanov et al., 1995), the IgE/Antigen receptor (Laffargue et al., 2002), receptor tyrosine kinases (RTKs) (Schmid et al., 2011), and the Toll-like receptors (TLRs) (Luo et al., 2018; Luo et al., 2014). Activation of PI3K $\gamma$  downstream of these stimuli are potentiated by their p84 and p101 regulatory subunits (Bohnacker et al., 2009; Luo et al., 2018; Stephens et al., 1997; Vadas et al., 2013; Kurig et al., 2009). In mouse models, loss of PI3K $\gamma$  either genetically or pharmacologically is protective in multiple inflammatory diseases including cardiovascular disease (Patrucco et al., 2004), arthritis (Camps et al., 2005), Lupus (Barber et al., 2005), asthma (Collmann et al., 2013), pulmonary inflammation and fibrosis (Thomas et al., 2009; Campa et al., 2018), and metabolic syndrome (Breasson et al., 2017). PI3K $\gamma$  is also a driver of pancreatic ductal adenocarcinoma progression through immunomodulatory effects (Kaneda et al., 2016a), and targeting PI3K $\gamma$  in the immune system in combination with checkpoint inhibitors has shown promise in experimental cancer therapy (De Henau et al., 2016; Kaneda et al., 2016b).

Extensive biophysical and biochemical assays have identified many of the molecular mechanisms underlying PI3K $\gamma$  regulation. The p110 $\gamma$  enzyme is composed of five domains, a putative uncharacterised adaptor binding domain (ABD), a Ras binding domain (RBD), a C2 domain, a helical domain, and a bi-lobal lipid kinase domain (Walker et al., 1999; Figure 1A). PI3K $\gamma$  activation is primarily mediated by G $\beta\gamma$  subunits downstream of GPCR signalling, through a direct interaction of G $\beta\gamma$  with the C2-helical linker of p110 $\gamma$  (Vadas et al., 2013). Activation of PI3K $\gamma$  by G $\beta\gamma$  requires a secondary interaction between G $\beta\gamma$  and regulatory subunits for physiologically relevant activation (Stephens et al., 1997), with the free p110 $\gamma$  subunit having no detectable activation downstream of GPCR activation in cells (Deladeriere et al., 2015). In addition, PI3K $\gamma$  activation can be facilitated by Ras GTPases interacting with the RBD of p110 $\gamma$  (Pacold et al., 2000), with the same interface also putatively mediating activation by Rab8 (Luo et al., 2014). Experiments exploring a novel type II-like kinase inhibitor that targets an active conformation of PI3K $\gamma$  revealed novel molecular aspects of regulation involving the C-terminal regulatory motif of the kinase domain, which is composed of the  $\alpha$ 7, 8, 9, 10, 11, 12 helices that surround the activation loop, and keep the enzyme in an inhibited state (Gangadhara et al., 2019; Figure 1B). The  $\alpha$ 10,  $\alpha$ 11, and  $\alpha$ 12 helices are sometimes referred to as the regulatory arch (Vadas et al., 2011). Inhibition mediated by the C-terminal regulatory motif is conserved through all class I PI3Ks, although for all other isoforms, this inhibited conformation requires interactions with a p85 regulatory subunit (Figure 1—figure supplement 1A +B; Burke, 2018). The activation of all class I PI3Ks is proposed to require a conformational change in the regulatory motif leading to a reorientation of the C-terminus to a conformation that is compatible with membrane binding (Figure 1—figure supplement 1C; Burke, 2018). The p110 $\gamma$  catalytic subunit is unique in that it maintains an inactive conformation in the absence of regulatory subunits. This conformation is proposed to be maintained by a Tryptophan lock, where W1080 maintains a closed conformation of the membrane binding C-terminal  $\alpha$ 12 helix, leading to an inactive conformation of the activation loop (Gangadhara et al., 2019; Figure 1B+D).

Disruption of PI3K signalling by either activating or inactivating mutations and deletions are involved in multiple human diseases. Overexpression of any activated class I PI3K isoform can lead to oncogenic transformation (Kang et al., 2006), although p110 $\alpha$  is the most frequently mutated in human disease. Activating p110 $\alpha$  mutations are linked to both cancer (Samuels et al., 2004; Vasan et al., 2019) and overgrowth disorders (Lindhurst et al., 2012), while activating p110 $\delta$  mutations are linked to primary immuno-deficiencies (Dornan et al., 2017; Lucas et al., 2016; Angulo et al., 2013). A high proportion of these activating mutations cluster to the C-terminal regulatory motif of the p110 catalytic subunits. Multiple p110 $\gamma$  mutations have been identified in cancer

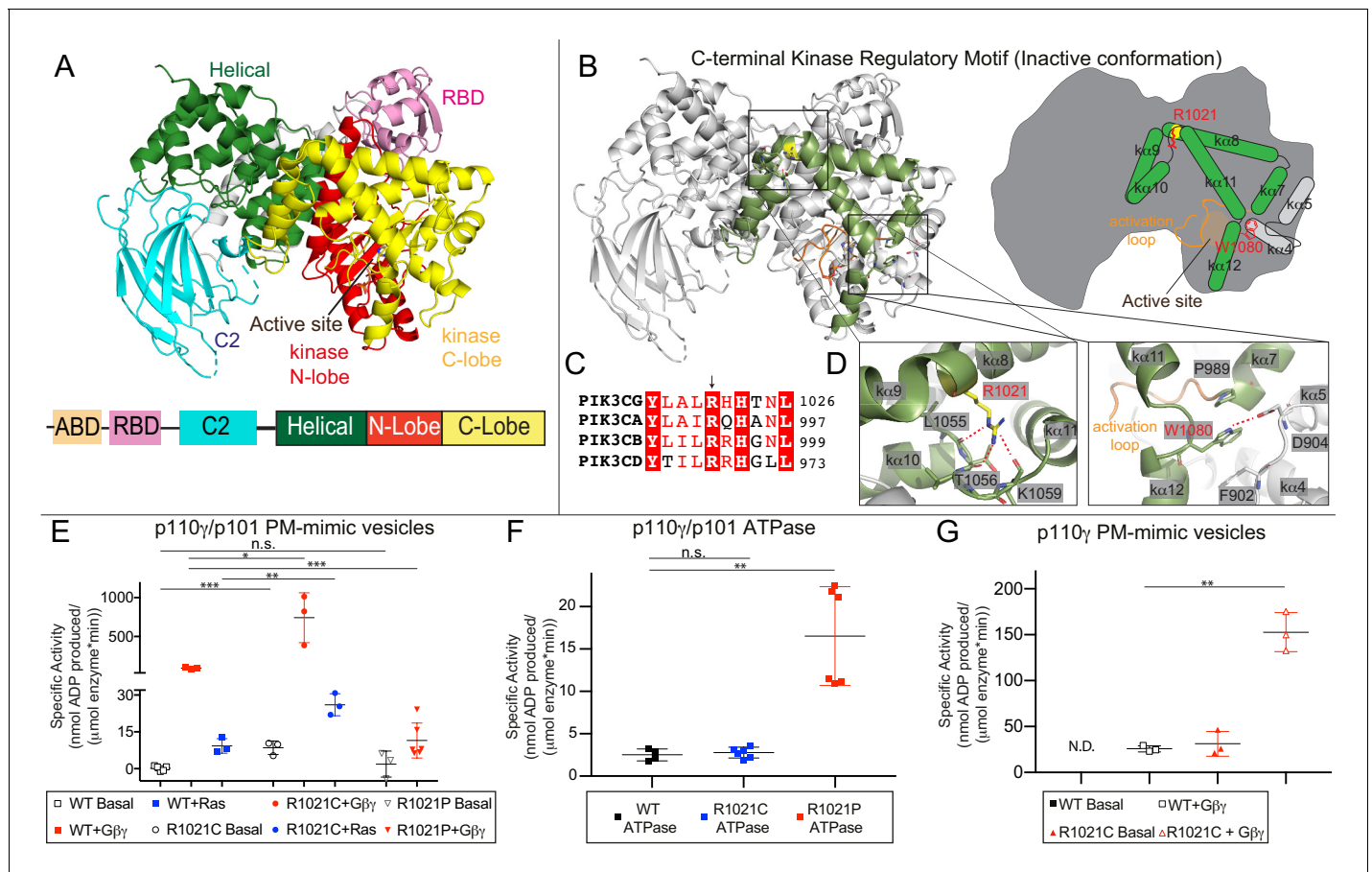


**Figure 1.** Mutations in the regulatory C-terminal motif of the kinase domain alter PI3K $\gamma$  activity. (A) Domain architecture of p110 $\gamma$  (PDB ID: 6AUD) (Safina et al., 2017), with the domain schematic shown beneath. (B) Model of the C-terminal regulatory motif of the kinase domain of p110 $\gamma$ . The helices that make up the regulatory motif, which includes the regulatory arch ( $\alpha$ 10, 11, 12) and those that pack against them ( $\alpha$ 7, 8, 9) are highlighted in green both in the structural model and cartoon schematic. (C) Alignment of residues around R1021 in p110 $\gamma$  with class IA p110 isoforms. (D) A close up of the W1080 'Tryptophan lock' interaction with  $\alpha$ 7 and the  $\alpha$ 4- $\alpha$ 5 loop which maintains an inhibited conformation is shown, as well as the interaction of the R1021 residue with residues on the  $\alpha$ 10- $\alpha$ 11 loop. (E) Lipid kinase activity assays testing the activity of WT, R1021C, and R1021P p110 $\gamma$ /p101 WT basally and in the presence of lipidated G $\beta$  $\gamma$  and HRas. Experiments were carried out with 50–3000 nM kinase, 1500 nM Ras, 1500 nM G $\beta$  $\gamma$ , all in the presence of 100  $\mu$ M ATP and 1 mg/mL PM-mimic vesicles 5% phosphatidylinositol 4,5 bisphosphate (PIP<sub>2</sub>), 20% phosphatidylserine (PS), 10% phosphatidyl choline (PC), 50% phosphatidylethanolamine (PE), 10% Cholesterol, 5% sphingomyelin (SM). (F) Activity assays testing the intrinsic ATPase activity (ATP conversion in the absence of membrane substrate) for wild type and mutant p110 $\gamma$ /p101 complexes. (G) Lipid kinase activity assays testing the activity of WT and R1021C for the free p110 $\gamma$  catalytic subunit with and without lipidated G $\beta$  $\gamma$ . Lipid kinase activity was generated by subtracting away non-specific ATPase activity, for unstimulated WT p110 $\gamma$  there was no detectable lipid kinase activity above basal ATPase activity (N. D.). For panels E-G every replicate is plotted, with error shown as standard deviation (n = 3–6). Two tailed p-values represented by the symbols as follows: \*\*\*<0.001; \*\*<0.01; \*<0.05; n.s. > 0.05. Refer to the **Figure 1—source data 1** file for the specific activity values.

The online version of this article includes the following source data and figure supplement(s) for figure 1:

**Source data 1.** Summary of HDX-MS data sets (see attached excel source data files).

**Figure supplement 1.** Comparing the different regulatory mechanisms that maintain the C-terminal regulatory motif in a inhibited state in the class I PI3Ks.

**Figure supplement 2.** Purification of mutated p110 $\gamma$  / p101 complexes.

patients (Lowery et al., 2019; AACR Project GENIE Consortium, 2017; Tate et al., 2019), although at a lower frequency than p110 $\alpha$  mutations. It would be expected that these mutations are activating, although this has not been fully explored. Intriguingly, p110 $\gamma$  loss-of-function mutations in the C-terminal regulatory motif (R1021P, N1085S) have been identified in patients with immunodeficiencies (Takeda et al., 2019; Thian et al., 2020; Figure 1B). PI3K mediated diseases being caused by both activating and inactivating mutations highlights the critical role of maintaining appropriate PIP<sub>3</sub> levels for human health.

The involvement of activated PI3K signalling in multiple diseases has motivated class I PI3K inhibitor development. There are, however, toxicity effects associated with compounds that target all PI3K isoforms by mechanism-based adverse side effects (*Fruman and Rommel, 2014*), driving the development of isoform selective inhibitors. These efforts have led to multiple clinically approved inhibitors of PI3K $\alpha$  and PI3K $\delta$  (*André et al., 2019; Brown et al., 2014; Flinn et al., 2014*). The critical role of PI3K $\gamma$  in inflammation and the tumour microenvironment has stimulated development of PI3K $\gamma$  specific inhibitors. Two main strategies for generating p110 $\gamma$  selective ATP-competitive inhibitors have been established: (i) targeting p110 $\gamma$ -specific pockets in and around the ATP-binding site which are not conserved among p110 isoforms (*Collier et al., 2015; Evans et al., 2016*), and (ii) targeting selective p110 $\gamma$  conformational changes (*Gangadhara et al., 2019*). Intriguingly, the conformational selective p110 $\gamma$  inhibitors appear to target its putatively activated conformation.

The parallel discovery of disease linked mutations in the C-terminal regulatory motif, and conformational selective p110 $\gamma$  inhibitors that cause altered dynamics of the C-terminus led us to investigate the underlying molecular mechanisms. Using a combined biochemical and biophysical approach, we characterised the dynamic conformational changes caused by the loss-of-function R1021P p110 $\gamma$  mutation, as well as a putative oncogenic R1021C p110 $\gamma$  mutation identified in the Catalogue of Somatic Mutations in Cancer database (COSMIC; *Tate et al., 2019*). We found that the R1021P mutant leads to greatly decreased protein stability, while the activating R1021C mutation leads to localised conformational disruption of the regulatory motif at the c-terminus. A screen of a number of PI3K $\gamma$  selective and pan-PI3K inhibitors revealed that many of these molecules induced allosteric conformational changes in p110 $\gamma$ . A combined X-ray crystallography and hydrogen deuterium exchange mass spectrometry (HDX-MS) approach showed that inhibitor interactions with the activation loop mediates the allosteric conformational changes. Intriguingly, similar conformational changes occurred with the R1021C mutant. The R1021C mutant was also found to be more sensitive to inhibition by kinase inhibitors that cause allosteric conformational changes. Overall, this work provides a unique insight into how mutations alter PI3K $\gamma$  regulation, and paves the way to novel strategies for isoform and mutant selective PI3K inhibitors.

## Results

### R1021P and R1021C mutations alter the activity of p110 $\gamma$

The recent discovery of an inactivating disease-linked mutation in *PIK3CG* located near the C-terminus of the p110 $\gamma$  kinase domain (R1021P) in immunocompromised patients led us to investigate the molecular mechanism of this mutation. Intriguingly, this same residue is found to be mutated in the COSMIC database (R1021C) (*Tate et al., 2019*). The R1021 residue in p110 $\gamma$  is conserved across all class I PI3K isoforms (*Figure 1C*), and mutations in the equivalent residue in *PIK3CA* (p110 $\alpha$ ) are putatively oncogenic (R992L/N) (*Tate et al., 2019*). To define the effect of these mutations on protein conformation and biochemical activity, we generated them recombinantly in complex with the p101 regulatory subunit. Both the p110 $\gamma$  R1021C and R1021P complexes with p101 eluted from gel filtration similar to wild-type p110 $\gamma$ -p101, suggesting they were properly folded (*Figure 1—figure supplement 2*). However, the yield of the R1021P complex with p101 was dramatically decreased relative to both wild-type and R1021C p110 $\gamma$ , indicating that this mutation may decrease protein stability, consistent with decreased p110 $\gamma$  and p101 expression in patient tissues (*Takeda et al., 2019*). We also generated the free R1021C p110 $\gamma$  subunit, however we could not express free p110 $\gamma$  R1021P, further highlighting that this mutation likely leads to decreased protein stability.

The R1021 residue forms hydrogen bonds with the carbonyl oxygens of L1055, T1056, and K1059 located in or adjacent to the regulatory arch helices  $\alpha$ 10 and  $\alpha$ 11 of PI3K $\gamma$  (*Figure 1D*). Both R1021C and R1021P would be expected to disrupt these interactions, with the R1021P also expected to distort the secondary structure of the  $\alpha$ 8 helix. The R1021P has been previously found to lead to greatly decreased lipid kinase activity in vitro (*Takeda et al., 2019*). To characterise these mutations, we carried out biochemical assays of wild-type, R1021C, and R1021P p110 $\gamma$ /p101 complexes against plasma membrane-mimic lipid vesicles containing 5% PIP<sub>2</sub>. Assays were carried out in the presence and absence of lipidated G $\beta$  $\gamma$  and Ras. Lipidated G $\beta$  $\gamma$  leads to a > 100-fold activation of lipid kinase activity for wild-type complexes, with Ras causing a ~ 10-fold activation. These assays revealed that p110 $\gamma$ /p101 R1021C was ~eightfold more active than wild-type both basally and in the



presence of G $\beta\gamma$ , and ~two- to threefold more active upon Ras activation (**Figure 1E**). The R1021C mutant also showed a ~eightfold increase in lipid kinase activity compared to wild-type when assaying the free p110 $\gamma$  subunit (**Figure 1G**). This is consistent with the R1021C mutation destabilising the regulatory motif, potentially disrupting the Tryptophan lock and leading to increased membrane recruitment.

The R1021P complex showed weak but detectable basal lipid kinase activity; however, there was almost no activation by lipidated G $\beta\gamma$  compared to wild-type, suggesting this complex would be almost completely inactive in a physiological context (**Figure 1E**). To examine if the catalytic machinery of the R1021P mutant was intact, we carried out experiments looking at ATPase activity (non-productive turnover of ATP in the absence of lipid substrate). Intriguingly, R1021P p110 $\gamma$ -p101 showed higher basal ATPase activity compared to wild-type p110 $\gamma$ /p101 and R1021C p110 $\gamma$ -p101, revealing that it still has catalytic activity, but almost no activity on membrane substrate (**Figure 1F**). This suggests that the minimal structural features required for ATP hydrolysis are maintained in the R1021P mutant, but that either membrane binding or PIP<sub>2</sub> recognition is severely impaired.

### R1021P and R1021C cause allosteric conformational changes throughout the regulatory C-terminal motif

We carried out hydrogen deuterium exchange mass spectrometry (HDX-MS) experiments to define the molecular basis for why two different mutations at R1021 have opposing effects on lipid kinase activity. HDX-MS is a technique that measures the exchange rate of amide hydrogens, and as the rate is dependent on the presence and stability of secondary structure, it is an excellent probe of protein conformational dynamics (*Vadas et al., 2017*). HDX-MS experiments were performed on complexes of wild-type p110 $\gamma$ /p101, R1021C p110 $\gamma$ /p101, and R1021P p110 $\gamma$ /p101, as well as the free wild-type and R1021C p110 $\gamma$ . The coverage map of the p110 $\gamma$  and p101 proteins was composed of 153 peptides spanning ~93% percent of the exchangeable amides (**Supplementary file 1**).

The R1021C and R1021P mutations led to significant changes in the conformational dynamics of the p110 $\gamma$  catalytic and p101 regulatory subunits (**Figure 2A–G**). The R1021P mutation resulted in large increases in exchange throughout almost the entire C2, helical, and kinase domains (**Figure 2B +D**). Comparing the rates of hydrogen exchange between wild-type, R1021C, and R1021P showed many regions where both R1021C and R1021P mutations caused increased H/D exchange. However, for the majority of these regions, the R1021P mutation led to increased exchange at early (3 s) and late timepoints (3000 s) of exchange, indicating that this mutation was leading to significant disruption of protein secondary structure (**Figure 2G**). This large-scale destabilisation throughout the protein may explain the low yield and decreased kinase activity.

The R1021C mutation resulted in increased H/D exchange in the C2, helical and kinase domains of p110 $\gamma$ . Intriguingly, many of the changes in dynamics of the helical and kinase domains are similar to those observed upon membrane binding (*Vadas et al., 2013*). The largest differences occurred in the helices in the C-terminal regulatory motif ( $\alpha 7$ –12) (**Figure 2A+C**). A peptide spanning the C-terminal end of the activation loop and  $\alpha 7$  (976–992) showed increased exchange, with these changes primarily occurring at later timepoints of exchange (3000 s) (**Figure 2G**). This is indicative of these regions maintaining secondary structure, although with increased flexibility. These increases in exchange for the R1021C mutant were conserved for the free p110 $\gamma$  subunit, although with larger increases in exchange compared to the p110 $\gamma$ /p101 complex (**Figure 2—figure supplement 1A–C**). Intriguingly, we found larger decreases in exchange with the p101 subunit for the R1021C p110 $\gamma$  compared to WT p110 $\gamma$ , which suggests a global stabilisation by the p101 subunit that mitigates some of the effects of the R1021C mutant (**Figure 2—figure supplement 1E+F**). Differences in HDX-MS with R1021C is consistent with a disruption of the inhibitory conformation of the regulatory motif. In addition, the increased dynamics of the activation loop seen in the mutant may pre-organise the catalytic machinery for activation. This is consistent with previous HDX-MS analysis of the regulatory mechanisms of class IA PI3Ks which revealed that increased dynamics of the activation loop occurred concurrently with increased lipid kinase activity (*Dornan et al., 2017; Dornan and Burke, 2018; Burke and Williams, 2013; Burke et al., 2012; Burke et al., 2011*).

The two mutations in R1021C and R1021P both caused increased exchange in the p101 subunit. Peptides spanning 602–623, and 865–877 of p101 showed similar increases in exchange for both R1021C and R1021P, with R1021P also leading to increased exchange in a peptide nearer the N-terminus (102–122) (**Figure 2E+F, S3D**). As there is no structural model for the p101 subunit, it is hard

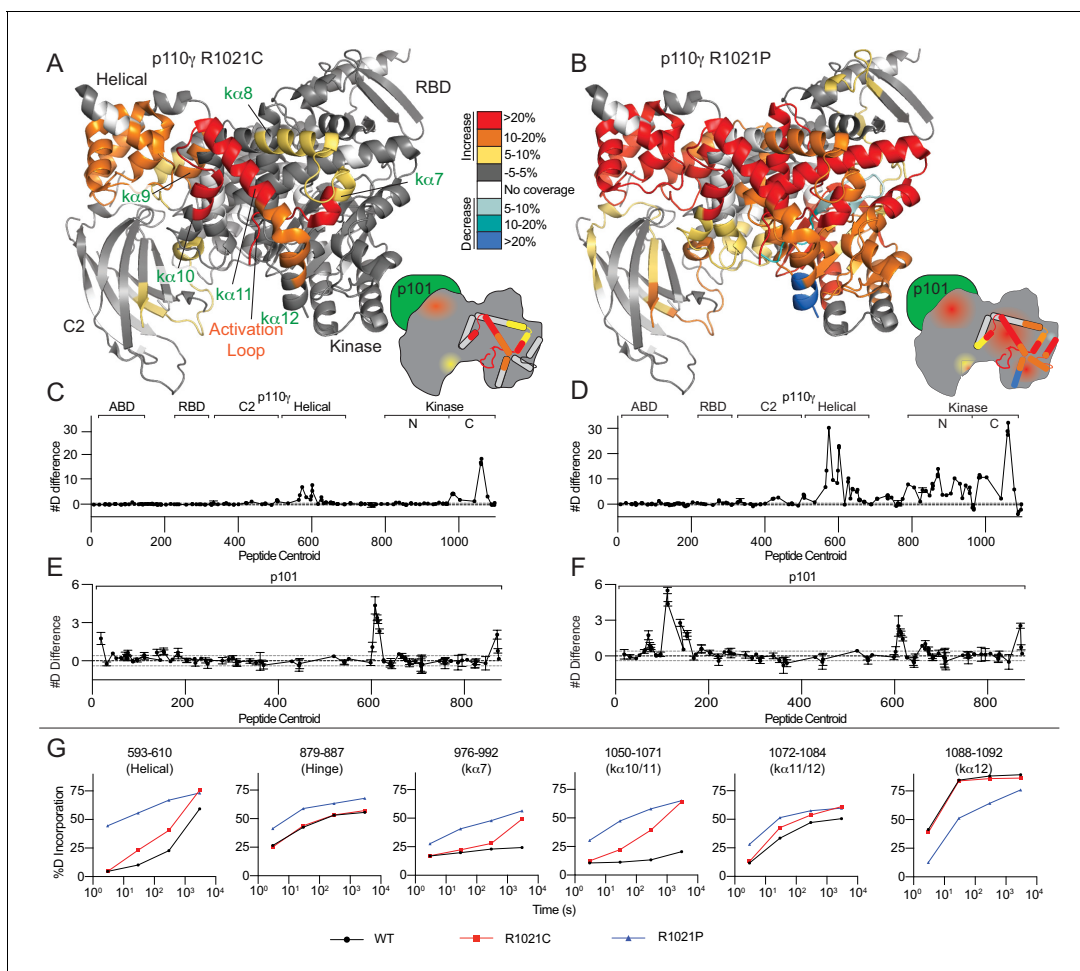


**Figure 2.** R1021C and R1021P mutations in p110 $\gamma$  are destabilising, with R1021P leading to global destabilisation and R1021C leading to localised disruption of the C-terminal regulatory W1080 Tryptophan 'lock'. (A+B) Peptides showing significant deuterium exchange differences (>5%, >0.4 kDa and  $p < 0.01$  in an unpaired two-tailed t-test) between wild-type and R1021C (A) and wild-type and R1021P (B) p110 $\gamma$ /p101 complexes are coloured on a model of p110 $\gamma$  (PDB: 6AUD) (Safina et al., 2017). Differences in exchange are coloured according to the legend. (C+D) The number of deuterium difference for the R1021C and R1021P mutants for all peptides analysed over the entire deuterium exchange time course for p110 $\gamma$ . Every point represents the central residue of an individual peptide. The domain location is noted above the primary sequence. A cartoon model of the p110 $\gamma$  structural model is shown according to the legend in panels A+B. Error is shown as standard deviation ( $n = 3$ ). (E+F) The number of deuterium difference for the R1021C and R1021P mutants for all peptides analysed over the entire deuterium exchange time course for p101. Every point represents the central residue of an individual peptide. Error is shown as standard deviation ( $n = 3$ ). (G) Selected p110 $\gamma$  peptides that showed decreases and increases in exchange are shown. The HDExaminer output data and the full list of all peptides and their deuterium incorporation is shown in the **Figure 2—source data 1** file.

The online version of this article includes the following source data and figure supplement(s) for figure 2:

**Source data 1.** Source data for HDX-MS comparing p110 $\gamma$ /p101 and mutants.

**Figure supplement 1.** Differences in HDX for the R1021C mutation in free p110 $\gamma$ .

**Figure supplement 1—source data 1.** Source data for HDX-MS comparing free p110 $\gamma$  and free p110 $\gamma$  R1021C.

to unambiguously interpret this data; however, these may represent increased H/D exchange due to partial destabilisation of the complex.

### Molecular dynamics of p110 $\gamma$ R1021C and R1021P mutants

We carried out Gaussian-accelerated Molecular Dynamics (GaMD) simulations of wild-type p110 $\gamma$  and its R1021C and R1021P variants to provide additional insight into the underlying molecular mechanisms of altered H/D exchange behaviour and different lipid kinase activity. Using the crystallographic structure of p110 $\gamma$  lacking the N-terminus [amino acids 144–1102, PDB: 6AUD

(Safina et al., 2017)], we generated the activation loop and other neighbouring loops as described in the methods, removed the co-crystallised ligand, and mutated R1021 to a cysteine and proline, resulting in three systems: WT, R1021C, and R1021P. Three replicas of fully solvated all-atom GaMD simulations were run for each model with AMBER18 achieving a cumulative extensive sampling of ~3, ~4.1, and ~1.5  $\mu$ s for WT, R1021C, and R1021P, respectively (Figure 3A+B).

To quantify the effect of mutations on the structural dynamics of p110 $\gamma$ , we calculated the root-mean-square-fluctuation (RMSF) of residues neighbouring the mutation site. RMSF was calculated to determine average flexibility of each residue's C $\alpha$  and C $\beta$  atoms around their mean position (Figure 3C). This revealed increased fluctuations in the residues forming the loop between  $\kappa\alpha 10$  and  $\kappa\alpha 11$  in the mutated systems, specifically residues T1056, V1057, and G1058 at the C-terminus of  $\kappa\alpha 10$ . Many of these residues participate in hydrogen bonds with R1021 in WT (Figure 3B).

Analysis of the simulations revealed that mutation of R1021 results in disruption of the hydrogen bonding network between R1021 and L1055, T1056, and K1059 in the  $\kappa\alpha 10$ - $\kappa\alpha 11$  region. There were also alterations in the intra and inter helix hydrogen bonds in  $\kappa\alpha 8$ ,  $\kappa\alpha 9$ ,  $\kappa\alpha 10$ , and  $\kappa\alpha 11$  (Figure 3D, S4). Hydrogen bonding occupancies between Y1017 and T1056 decreased from 71% in WT to 56% and 45% in the R1021C and R1021P systems, respectively. Examining the  $\kappa\alpha 8$ - $\kappa\alpha 9$  backbone hydrogen bonding at the site of mutation, both mutations showed a disruption between C/P1021 and T1024. Additionally, the proline mutation showed complete disruption of backbone hydrogen bonds at A1016-L1020 and Y1017-P1021, decreased bonding occupancy at K1015-A1019

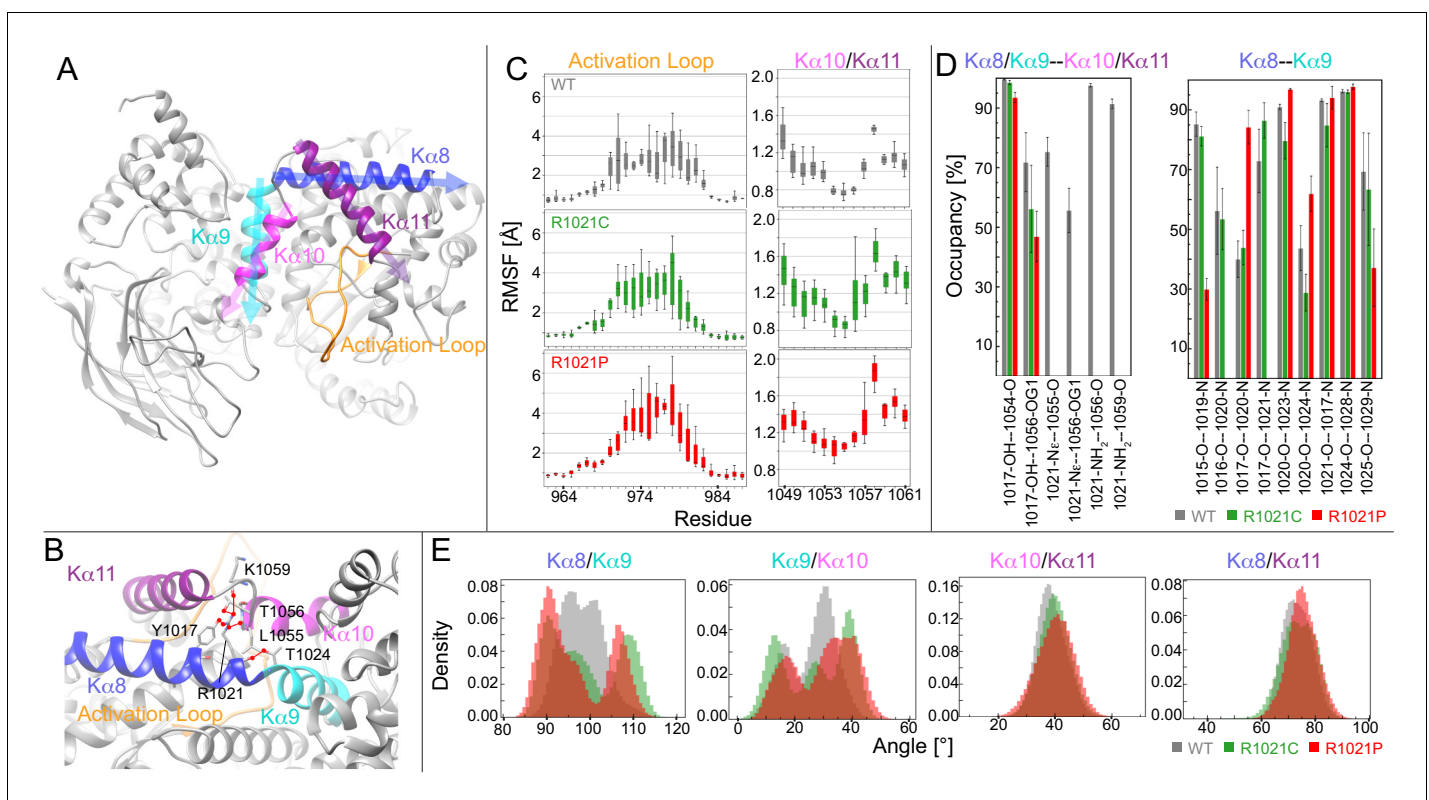


**Figure 3.** Molecular dynamic simulations reveal that the R1021C and R1021P mutations show increased instability in p110 $\gamma$ . (A) Model of p110 $\gamma$  showcasing the regulatory domain's  $\kappa\alpha 8$  (995–1023),  $\kappa\alpha 9$  (1024–1037),  $\kappa\alpha 10$  (1045–1054), and  $\kappa\alpha 11$  (1057–1078) helices, and the activation loop (962–988). (B) A zoomed-in snapshot of R1021 microenvironment showing residues in licorice. Hydrogen bonds with R1021 are drawn as red lines. (C) RMSF [Å] of each residue's C $\alpha$  and C $\beta$  atoms in the activation loop and the  $\kappa\alpha 10/\kappa\alpha 11$  helices, respectively. RMSF values for each atom across replicates are shown as a quantile plot, with error shown as standard deviation ( $n = 3$ ). (D) The mean and standard deviation of hydrogen bond occupancies between the indicated helices/sets of helices across replicates ( $n = 3$ ). (E) Inter-angle density distributions across all replicas between  $\kappa\alpha 8$ ,  $\kappa\alpha 9$ ,  $\kappa\alpha 10$ , and  $\kappa\alpha 11$ . In all panels, WT, R1021C, and R1021P are coloured in grey, green, and red, respectively.

The online version of this article includes the following figure supplement(s) for figure 3:

**Figure supplement 1.** Differences between molecular dynamic simulations of WT, R1021C, and R1021P.

and N1025-I1029, and increased bonding occupancy of Y1017-L1020 and P1021-T1024. The notable increase in hydrogen bonding disruption in the R1021P compared to R1021C could be responsible for the increased destabilisation observed by HDX-MS.

To obtain further insights into the dynamic behaviour of the C-terminus of the kinase domain and how mutation of R1021 alters conformational dynamics, we monitored the fluctuations of four different angles formed between  $\kappa\alpha 8$ ,  $\kappa\alpha 9$ ,  $\kappa\alpha 10$ , and  $\kappa\alpha 11$  (Figure 3E). The simulations revealed increased angle fluctuations in the mutant simulations between  $\kappa\alpha 8$  and  $\kappa\alpha 9$ , and  $\kappa\alpha 9$  and  $\kappa\alpha 10$ , with a bimodal distribution in the  $\kappa\alpha 8/\kappa\alpha 9$  angle compared to WT. There was also increased fluctuations in the activation loop in the mutants compared to WT (Figure 3C, Figure 3—figure supplement 1). We did not observe large-scale conformational disruption in the R1021P mutant, which may require more extensive MD timescales to observe global stability differences. Overall, the MD, HDX-MS, and kinase assays are consistent with the R1021C mutation altering the dynamics of the regulatory motif, and destabilizing the region around the tryptophan lock. This region must open to allow for membrane binding (Vadas et al., 2013), suggesting that this mutation may pre-organise the regulatory motif for membrane binding/catalysis.

### Multiple PI3K $\gamma$ inhibitors lead to allosteric conformational changes

The increased H/D exchange in the regulatory motif for the R1021C mutant is similar to previously observed differences caused by cyclopropyl ethyl containing isoindolinone inhibitors (Gangadhara et al., 2019). This result suggested it would be worth interrogating the dynamics of p110 $\gamma$  induced by multiple classes of p110 $\gamma$  inhibitors. Specifically, we wanted to understand if inhibitors that promote allosteric conformational changes might be useful in the development of isoform/mutant selective compounds.

We performed HDX-MS experiments with seven potent PI3K inhibitors on free p110 $\gamma$  to define the role of allostery in PI3K $\gamma$  inhibition. We analysed inhibitors that were selective for PI3K $\gamma$  (AS-604850 [Camps et al., 2005], AZ2 [Gangadhara et al., 2019], NVS-PI3-4 [Collmann et al., 2013; Bruce et al., 2012], and IPI-549 [Evans et al., 2016]) as well as pan-PI3K inhibitors (PIK90 [Knight et al., 2006], Omipalisib [Knight et al., 2010], and Gedatolisib [Venkatesan et al., 2010]). Of these compounds, only AS-604850, PIK90, and Omipalisib have been structurally characterised bound to p110 $\gamma$ . A table summarizing these compounds and their selectivity for different PI3K isoforms is shown in Supplementary file 5. Deuterium exchange experiments were carried out with monomeric p110 $\gamma$  over 4 timepoints of deuterium exchange (3,30,300, and 3000 s). We obtained 180 peptides covering ~89% percent of the exchangeable amides (Supplementary file 2). To verify that results on the free p110 $\gamma$  complex are relevant to the physiological p110 $\gamma$ /p101 complex, we also carried out experiments with the p110 $\gamma$ /p101 complex with Gedatolisib and IPI-549, with the free p110 $\gamma$  showing almost exactly the same differences as seen for the p110 $\gamma$ /p101 complex (Figure 4—figure supplement 1).

Based on the H/D exchange differences observed with inhibitors present, we were able to classify the inhibitors into three broad groups. The first group contains the isoquinolinone compound IPI-549, the imidazo[1,2-c]quinazoline molecule PIK-90 and the thiazolidinedione compound AS-604850 (Figure 4A+B). These compounds caused decreased exchange near the active site, with the primary protected region being the hinge region between the N- and C-lobes of the kinase domain (Figure 4B+E). No (IPI-549, AS-604850) or very small (PIK-90) increases in deuterium incorporation were observed (Figure 4A, Figure 4—figure supplement 2A–C), suggesting that there are localised allosteric conformational changes for these compounds.

The H/D exchange experiments revealed a second class of inhibitors that showed decreased exchange at the active site, but also significant increases in exchange in the kinase and helical domains (Figure 4A+C, Figure 4—figure supplement 2D–F). The second group includes the bismorpholinotriazine molecule Gedatolisib, difluoro-benzene sulfonamide compound Omipalisib, and the PI3K $\gamma$ -specific thiazole derivative NVS-PI3-4. Binding of these inhibitors caused increased exchange in multiple regions of the kinase regulatory motif, including  $\kappa\alpha 7$ ,  $\kappa\alpha 10$ ,  $\kappa\alpha 11$ , and  $\kappa\alpha 12$ . The peptide covering  $\kappa\alpha 7$  also spans the C-terminal end of the activation loop (Figure 4C+E). In addition to these changes, there were also increases in exchange within the helical domain. Intriguingly, for Gedatolisib, the regions of the protein that showed differences in H/D exchange matched very closely to those observed in the R1021C mutant. This suggests that the conformational changes



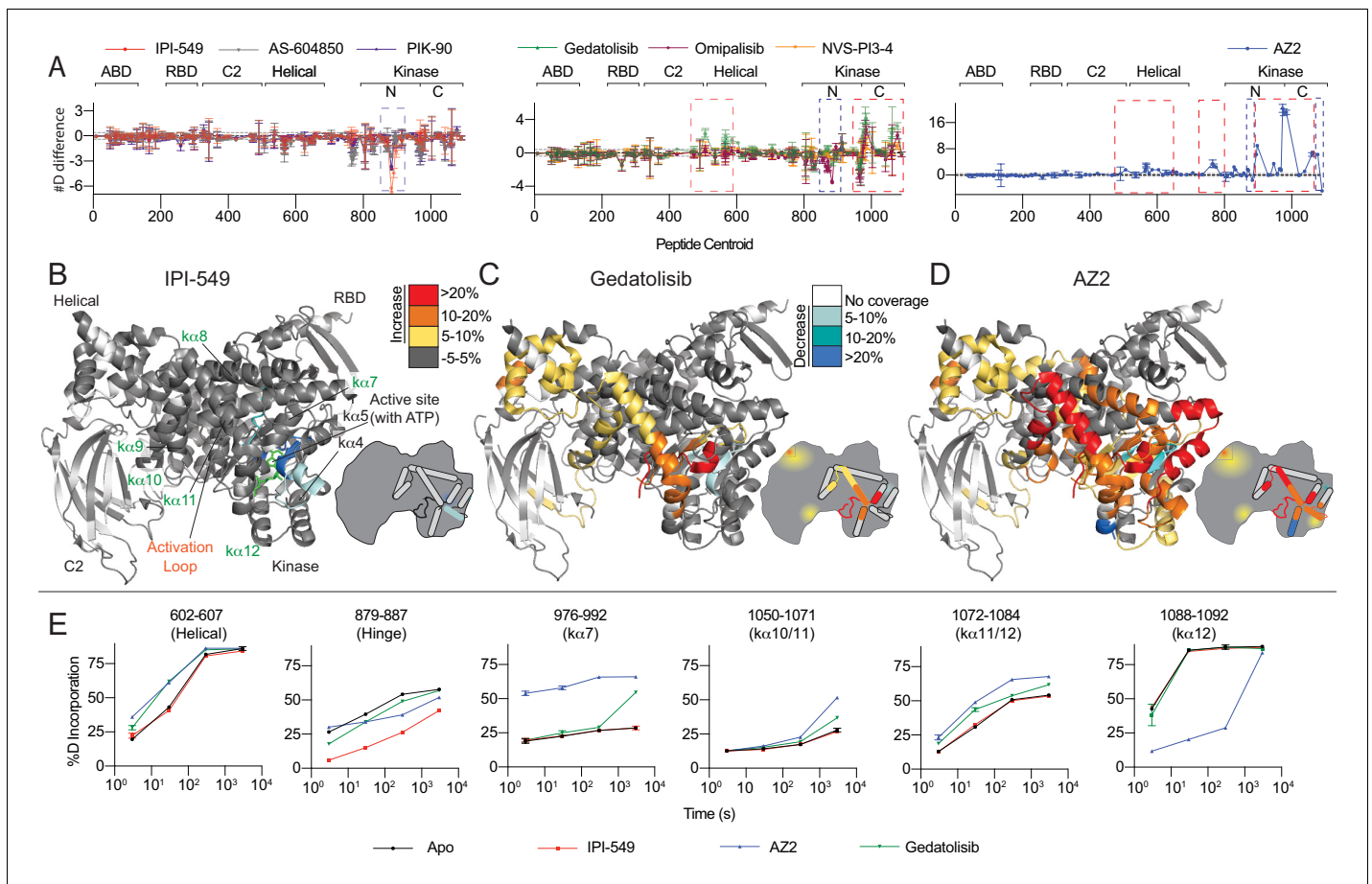


**Figure 4.** HDX-MS reveals that different classes of PI3K inhibitors lead to unique allosteric conformational changes. (A) The number of deuterium difference for the seven different inhibitors analysed over the entire deuterium exchange time course for p110 $\gamma$ . Every point represents the central residue of an individual peptide. The domain location is noted above the primary sequence. Error is shown as standard deviation ( $n = 3$ ). (B–D) Peptides showing significant deuterium exchange differences ( $>5\%$ ,  $>0.4$  kDa and  $p < 0.01$  in an unpaired two-tailed t-test) between wild-type and IPI-549 (B), Gedatolisib (C), and AZ2 (D) are coloured on a model of p110 $\gamma$  (PDB: 6AUD). Differences in exchange are mapped according to the legend. A cartoon model in the same format as **Figure 1** is shown as a reference. (E) Selected p110 $\gamma$  peptides that showed decreases and increases in exchange are shown. The HDXaminer output data and the full list of all peptides and their deuterium incorporation is shown in the **Figure 4—source data 1** file. The online version of this article includes the following source data and figure supplement(s) for figure 4:

**Source data 1.** Source data for HDX-MS comparing free p110g with and without inhibitors.

**Figure supplement 1.** Differences in HDX for free p110 $\gamma$  and p110 $\gamma$ /p101 with selected inhibitors.

**Figure supplement 1—source data 1.** Source data for HDX-MS comparing p110g/p101 with and without IPI-549/Gedatolisib.

**Figure supplement 2.** HDX-MS reveals that different classes of PI3K inhibitors lead to unique allosteric conformational changes.

induced by these compounds may partially mimic the activated state that occurs in the R1021C mutant.

Finally, AZ2 caused large-scale increased exposure throughout large regions of the helical and kinase domains (**Figure 4A+D**), consistent with previous reports (*Gangadhara et al., 2019*). The same regulatory motif regions that showed increased exchange with Gedatolisib showed much larger changes with AZ2. Importantly, increased exchange was observed at earlier timepoints for AZ2 compared to Gedatolisib (example peptide 976–992 covering the activation loop and  $k\alpha 7$ ), suggesting that AZ2 leads to a complete disruption of secondary structure, with Gedatolisib likely causing increased secondary structure dynamics (**Figure 4E**).

This shows that multiple PI3K inhibitors can cause large scale allosteric conformational changes upon inhibitor binding, however, deciphering the molecular mechanism of these changes were hindered by lack of high-resolution structural information for many of these compounds.

## Structures of PI3K $\gamma$ bound to IPI-549, Gedatolisib, and NVS-PI3-4

To further define the molecular basis for how different inhibitors lead to allosteric conformational changes, we solved the crystal structure of p110 $\gamma$  bound to IPI-549, Gedatolisib, and NVS-PI3-4 at resolutions of 2.55 Å, 2.65 Å, and 3.15 Å, respectively (**Figure 5A–C**, **Figure 5—figure supplement 1A–F**). The inhibitor binding mode for all were unambiguous (**Figure 5—figure supplement 2A**).

These structures revealed insights into how IPI-549 and NVS-PI3-4 can achieve selectivity for PI3K $\gamma$  (**Figure 5—figure supplement 1G–H**). All inhibitors formed the critical hydrogen bond with the amide hydrogen of V882 in the hinge region, which is a conserved feature of ATP competitive PI3K kinase inhibitors. NVS-PI3-4 leads to opening of a p110 $\gamma$  unique pocket mediated by a conformational change in K883 (**Figure 5—figure supplement 1G+H**). The opening of K883 is accommodated by it rotating into contact with D884 and T955. This opening would not be possible in p110 $\alpha$  and p110 $\delta$  as the corresponding K883 residue (L829 in p110 $\delta$  and R852 in p110 $\alpha$ ) would clash with the corresponding T955 residue (R902 in p110 $\delta$  and K924 in p110 $\alpha$ ) (**Figure 5—figure supplement 1I+J**). IPI-549 binds with a characteristic propeller shape, as seen for multiple p110 $\gamma$  and p110 $\delta$  selective inhibitors (**Berndt et al., 2010**). IPI-549 leads to a conformational change in the orientation of M804, which opens the specificity pocket, primarily composed of W812 and M804 (**Figure 5C**, **Figure 5—figure supplement 1D**). Comparison of IPI-549 bound to p110 $\gamma$  to the selective inhibitor Idelalisib bound to p110 $\delta$  revealed a potential molecular mechanism for p110 $\gamma$  selectivity. Structure activity analysis of IPI-549 and its derivatives showed a critical role for substitutions at the alkyne position in achieving p110 $\gamma$  specificity (**Evans et al., 2016**). The *N*-methylpyrazole group in IPI-549 projects out of the specificity pocket towards the  $\kappa\alpha 1$ - $\kappa\alpha 2$  loop. This loop is significantly shorter in

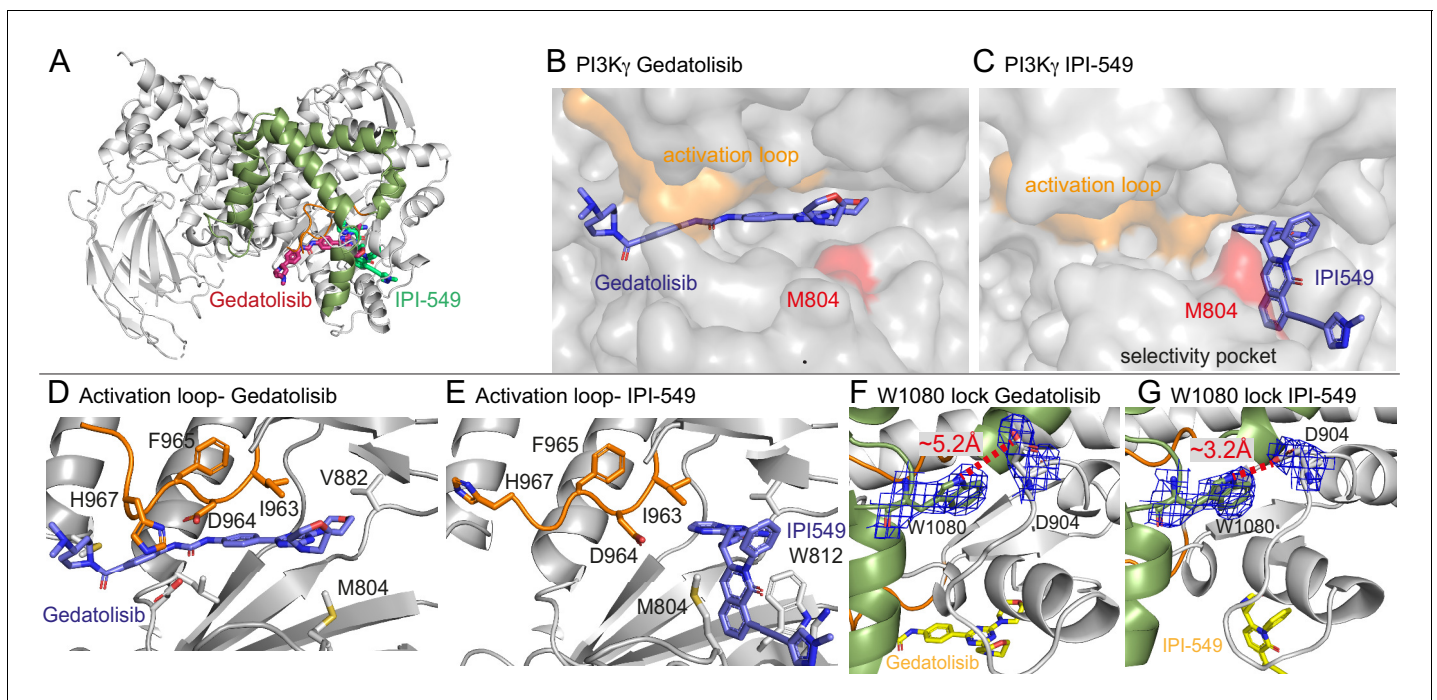


**Figure 5.** Structures of Gedatolisib and IPI-549 bound to p110 $\gamma$ . (A) Overall structure of Gedatolisib (red) and IPI-549 (green) bound to p110 $\gamma$ . (B–C) Comparison of Gedatolisib and IPI-549 bound to p110 $\gamma$  with the activation loop and selectivity pocket highlighted. M804 that changes conformation upon selectivity pocket opening is coloured red. (D–E) Comparison of the conformation of the activation loop (orange) of p110 $\gamma$  when Gedatolisib or IPI-549 are bound, with residues in the activation loop labelled, specifically D964 and F965 of the DFG motif labelled. (F–G) The Trp lock composed of W0180 is partially disrupted in the Gedatolisib structure compared to the IPI-549 structure. The interaction between W1080 and D904 is shown, with the distance between the two shown on each structure. The electron density from a feature enhanced map (**Afonine et al., 2015**) around W1080 and D904 in each structure is contoured at 1.5 sigma.

The online version of this article includes the following figure supplement(s) for figure 5:

**Figure supplement 1.** Structures of Gedatolisib, IPI-549, and NVS-PI3-4 bound to p110 $\gamma$ .

**Figure supplement 2.** Binding of IPI-549, NVS-PI3-4, and Gedatolisib lead to different conformations of the activation loop of p110 $\gamma$ .

p110 $\delta$ , with a potential clash with bulkier alkyne derivatives (**Figure 5—figure supplement 1K+L**). However, this cannot be the main driver of specificity, as a phenyl substituent of the alkyne had decreased selectivity for p110 $\gamma$  over p110 $\delta$ , with hydrophilic heterocycles in this position being critical in p110 $\gamma$  selectivity (**Evans et al., 2016**). A major difference in this pocket between p110 $\gamma$  and p110 $\delta$  is K802 in p110 $\gamma$  (T750 in p110 $\delta$ ), with this residue making a pi-stacking interaction with W812. The *N*-methylpyrazole group packs against K802, with a bulkier group in this position likely to disrupt the pi stacking interaction, explaining the decreased potency for these compounds (**Evans et al., 2016**).

One of the most striking differences between the structure of Gedatolisib and IPI-549 bound to p110 $\gamma$  is the conformation of the N-terminus of the activation loop, including the residues that make up the DFG motif (**Figure 5B–E, Figure 5—figure supplement 2B–F**). The majority of the activation loop is disordered in PI3K $\gamma$  crystal structures, with the last residue being between 967 and 969. Gedatolisib makes extensive contacts with the activation loop, with H967 immediately following the DFG motif in a completely altered conformation. The interaction of the cyclopropyl motif in AZ2 with the activation loop has previously been proposed to be critical in mediating allosteric conformational changes. In addition to the change in the activation loop, there was a minor perturbation of the W1080 lock, with the Gedatolisib structure revealing a disruption of the hydrogen bond between W1080 and D904, with this bond maintained in the IPI-549 structure (**Figure 5F+G**). The C-terminus of the activation loop and  $\kappa\alpha 7$  immediately following showed some of the largest changes upon inhibitor binding in HDX experiments. The  $\kappa\alpha 7$  helix is directly in contact with W1080, and we postulated that the conformational changes induced in the N-terminus of the activation loop may mediate these changes.

### Conformational selective inhibitors show altered specificity towards activating PI3K $\gamma$ mutant

We observed that HDX differences occurring in the R1021C mutant were very similar to conformational changes observed for p110 $\gamma$  bound to Gedatolisib. This suggests that both the mutant and Gedatolisib bound forms might be adopting an activated conformation of the regulatory motif. HDX differences were very similar for the region spanning 976–992 in the activation loop (**Figure 2G, Figure 4E**). As this region is directly adjacent to the inhibitor binding site, we postulated that there may be altered inhibitor binding for the R1021C mutant. We carried out IC<sub>50</sub> measurement for wild-type and R1021C p110 $\gamma$ /p101 with both IPI-549 and Gedatolisib (**Figure 6A**). Gedatolisib was roughly threefold more potent for the R1021C mutant over the wild-type, with no significant difference in IC<sub>50</sub> values for IPI-549 compared to wild-type. This provides initial insights into how understanding the dynamics of activating mutations and inhibitors may be useful as a novel strategy towards designing mutant specific inhibitors.

## Discussion

Understanding the molecular determinants of how mutations in PI3Ks lead to altered signalling in disease is vital in the design of targeted therapeutic strategies. The PI3K $\gamma$  isoform is critical to maintain immune system function, and plays important roles in the regulation of the tumour microenvironment (**Fruman et al., 2017; Okkenhaug, 2013**). Bi-allelic loss-of-function mutations in p110 $\gamma$  are a driver of human immunodeficiencies, and multiple inactivating mutations located in the C-terminal regulatory motif of the kinase domain have been described (**Takeda et al., 2019; Thian et al., 2020**). Initial results linking deletion of PI3K $\gamma$  to the development of colon cancer (**Sasaki et al., 2000b**) have been disputed (**Barbier et al., 2001**), and recent studies suggest that tumour growth and metastasis is attenuated in PI3K $\gamma$  deficient mice (**Kaneda et al., 2016b; Torres et al., 2019**) and IPI-549-treated animals (**De Henau et al., 2016**). Inhibiting PI3K $\gamma$  has shown promise as an immunomodulatory agent in generating an antitumour immune response (**De Henau et al., 2016; Kaneda et al., 2016b**). There have also been numerous reports of overexpression and single-nucleotide variants in *PIK3CG* linked to cancer development in multiple tissues (**Torres et al., 2019; Dituri et al., 2012; Edling et al., 2010; Ge et al., 2019; Zhang et al., 2019; Nava Rodrigues et al., 2018; Shu et al., 2018; Wang et al., 2020**). Oncogenic mutations in *PIK3CG* are widely distributed, which is distinct from the oncogenic hotspot mutations seen in the helical and kinase domain of *PIK3CA*. There has been limited analysis of the functional consequences of oncogenic *PIK3CG*

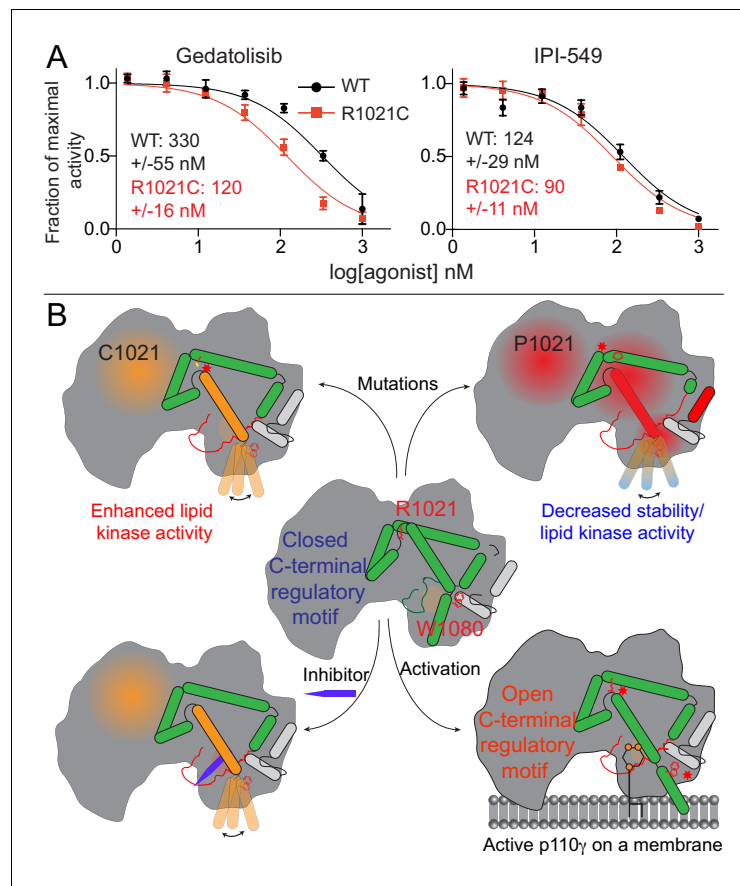


**Figure 6.** Activating mutations show slight differences in inhibition by allosteric inhibitors and model of PI3K $\gamma$  regulation. (A) IC<sub>50</sub> curves for wild-type and R1021C p110 $\gamma$ /p101 complexes. Assays were carried out with 5% C8 PIP<sub>2</sub>/95% PS vesicles at a final concentration of 1 mg/ml in the presence of 100  $\mu$ M ATP and 1.5  $\mu$ M lipidated G $\beta$  $\gamma$ . PI3K $\gamma$  concentration was 4 nM for R1021C and 8 nM for WT. Error is shown as standard deviation (n = 3). Refer to the **Figure 6—source data 1** file for IC<sub>50</sub> curve data. (B) Model of conformational changes that occur upon mutation of the C-terminal motif and binding of activation loop interacting conformation selective inhibitors. The online version of this article includes the following source data for figure 6:

**Source data 1.** Source data for IC<sub>50</sub> curves comparing inhibition of WT and R1021C p110 $\gamma$ /p101.

mutants, with the R1021 residue in the regulatory motif of the kinase domain being unique, as mutations of this residue exist in both immunodeficiencies and tumours.

Here, we have described the biochemical and biophysical characterisation of both activating and inactivating disease-linked R1021 mutations in the regulatory motif of the p110 $\gamma$  kinase domain. This has revealed that mutation of R1021 can lead to either kinase activation or inactivation. The R1021 in the  $\alpha$ 8 helix is conserved across all class I PI3Ks, with it making a number of hydrogen bonds with residues in  $\alpha$ 10 and  $\alpha$ 11. Both R1021P and R1021C would lead to disruption of the hydrogen bonds with  $\alpha$ 10 and  $\alpha$ 11, however R1021P would also lead to disruption of the  $\alpha$ 8 helix due to the altered dynamics introduced by the proline residue. HDX-MS results were consistent with this hypothesis, with R1021P leading to large-scale conformational changes across the entire protein, with the main disruptions occurring in the helical and kinase domain. The R1021P mutation greatly destabilised the protein, with purification yields being >20-fold lower than wild-type, consistent with greatly decreased p110 $\gamma$  and p101 levels in patient T cells (Takeda et al., 2019). Consistent with previous reports, we found greatly decreased lipid kinase activity for R1021P, although the enzyme maintained catalytic ability, as it showed greatly increased basal ATPase activity, which is similar to what occurs upon mutation of the W1080 lock or removal of the  $\alpha$ 12 helix (Gangadhara et al., 2019; Takeda et al., 2019). Overall, this data is consistent with this mutation leading to



destabilisation of the p110 $\gamma$  protein, leading to both greatly decreased protein levels, and decreased lipid kinase activity.

The R1021C mutation, in contrast, had enhanced lipid kinase activity, both basally, and upon G $\beta\gamma$  activation. HDX-MS and MD simulations suggest that this activation is mediated by a conformational disruption of the inhibitory c-terminal regulatory motif of the kinase domain. Many of these changes in the C-terminal regulatory motif have been previously observed upon membrane binding (Vadas *et al.*, 2013), as well as upon binding to conformational selective inhibitors (Gangadhara *et al.*, 2019). One of the largest changes in exchange occurred at the C-terminus of the activation loop and the beginning of  $\alpha 7$  which is in contact with the W1080 lock. We propose a model of how mutation of R1021 can lead to either activated or inactivated lipid kinase activity (Figure 6B). The conformation of the C-terminal regulatory motif is critical in regulating lipid kinase activity, where minor perturbations (R1021C) can lead to disruption of multiple inhibitory contacts allowing for reorientation of the  $\alpha 12$  membrane binding helix and increased lipid kinase activity. This suggests that the mutation can pre-organise the enzyme for productive catalysis, either through increased membrane binding, or increased PIP<sub>2</sub> kinase activity. Reinforcing the importance of the R1021 mutant for class I PI3K regulation is the fact that mutation of the equivalent R992 in PIK3CA to either Leu or Asn has been found in tumour samples (Tate *et al.*, 2019).

This work corroborates the important role of the C-terminal regulatory motif in controlling PI3K lipid kinase activity. The orientation of this motif is critical in the regulation of all class I PI3Ks, although this is regulated by different molecular mechanisms in p110 $\alpha$ , p110 $\beta$ , p110 $\delta$ , and p110 $\gamma$ . The class IA PI3Ks require p85 regulatory subunits to stabilise the C-terminal regulatory motif, with the nSH2 of p85 interacting with and stabilising  $\alpha 10$  for all class IA PI3Ks (Burke and Williams, 2013; Mandelker *et al.*, 2009), and the cSH2 of p85 stabilising  $\alpha 7$ ,  $\alpha 8$ ,  $\alpha 11$ , and  $\alpha 12$  for p110 $\beta$  and p110 $\delta$  (Burke *et al.*, 2011; Zhang *et al.*, 2011). The p110 $\gamma$  isoform is unique in that its C-terminal motif adopts an inhibited conformation in the absence of regulatory proteins. The C-terminal regulatory motif of p110 $\gamma$  can be post-translationally modified by phosphorylation of  $\alpha 9$  (T1024) by protein kinase A decreasing lipid kinase activity (Perino *et al.*, 2011), while protein kinase C phosphorylates an adjacent area in the helical domain (S582) (Walser *et al.*, 2013) increasing lipid kinase activity.

Extensive work has been carried out toward the development of allosteric inhibitors of PI3Ks. Although no allosteric inhibitors that bind out of the ATP-binding pocket have been developed, fragment screens have revealed potential druggable pockets that may be targeted in class IA PI3Ks (Miller *et al.*, 2017). It has previously been noted that PI3K $\gamma$  can be selectively targeted through a conformationally selective inhibitor, AZ2 (Gangadhara *et al.*, 2019). This was mediated through a cyclopropyl moiety on AZ2, which putatively alters the orientation of the activation loop, leading to disruption of the inhibitory conformation of the C-terminal regulatory motif. Many of the changes observed for this inhibitor were similar to those seen in the R1021C mutant. To interrogate if allosteric conformational changes were unique to cyclopropyl containing compounds, we screened a panel of pan-PI3K and PI3K $\gamma$  selective inhibitors using HDX-MS. The compounds PIK90, IPI549, and AS-604850 only caused decreased exchange at the active site. Comparison of the crystal structures of these compounds (Camps *et al.*, 2005; Knight *et al.*, 2006) revealed similar conformations of the activation loop, with limited interaction between the inhibitors and the activation loop. After submission of this manuscript, the structure of IPI-549 was released by Arcus Biosciences (Drew *et al.*, 2020) with a conserved binding mode to the model proposed here.

The AZ2 compound containing the cyclopropyl moiety, led to large-scale conformational changes consistent with previous results (Gangadhara *et al.*, 2019). Intriguingly, the non-specific inhibitors, Gedatolisib and Omipalisib, caused increased exchange in many of the same regions that showed enhanced exchange with the R1021C mutant. Comparison of the crystal structures of these inhibitors revealed more extensive interactions with the activation loop and significant conformational rearrangement of the activation loop. Distinct from the AZ2 compound, neither Gedatolisib and Omipalisib show specificity for PI3K $\gamma$  over class IA PI3Ks (Knight *et al.*, 2010; Venkatesan *et al.*, 2010). Similar HDX-MS differences were observed for both the R1021C mutant and wild type bound to Gedatolisib. Gedatolisib showed increased potency versus R1021C over wild-type PI3K $\gamma$ , with a ~ 3 fold decrease in IC<sub>50</sub> values. Altogether, this suggests that R1021C induces a conformation similar to the wild type enzyme bound to Gedatolisib. This provides an intriguing approach for designing

oncogenic PI3K-specific inhibitors through further optimisation of the ATP competitive inhibitor moieties in the activation loop binding region.

Overall, this work provides novel insights into how the C-terminal regulatory motif of PI3K $\gamma$  regulates lipid kinase activity, how oncogenic and immunodeficiency mutations can disrupt this regulation, and how one can exploit these conformational changes to develop isoform and mutant selective small molecule inhibitors. Further exploration of the dynamic regulation of the C-terminal regulatory motif of PI3Ks by mutations and inhibitors may reveal unique approaches to develop therapeutics for PI3K-related human diseases.

## Materials and methods

### Key resources table

Reagent type (species) or resource	Designation	Source or reference	Identifiers	Additional information
Cell Line ( <i>Spodoptera frugiperda</i> )	Sf9	Expression Systems	94-001S	Insect cell line for protein expression
Recombinant DNA reagent	pACEBac1-p110 $\gamma$ (plasmid)	This paper	MR30	PIK3CG Sf9 expression vector (available from Burke lab)
Recombinant DNA reagent	pACEBac1-p110 $\gamma$ R1021C (plasmid)	This paper	MR53	PIK3CG Sf9 expression vector (available from Burke lab)
Recombinant DNA reagent	pMultiBac-p110 $\gamma$ /p101(plasmid)	This paper	MR22	PIK3CG/PIK3R5 Sf9 expression vector (available from Burke lab)
Recombinant DNA reagent	pMultiBac-p110 $\gamma$ R1021C /p101(plasmid)	This paper	JS39	PIK3CG/PIK3R5 Sf9 expression vector (available from Burke lab)
Recombinant DNA reagent	pbiGBac-p110 $\gamma$ R1021P /p101(plasmid)	This paper	MR92	PIK3CG/PIK3R5 Sf9 expression vector (available from Burke lab)
Recombinant DNA reagent	pFastBac-HRas G12V (plasmid)	This paper	BS9	HRAS Sf9 expression vector (available from Burke lab)
Recombinant DNA reagent	pMultiBac-G $\beta$ 1/G $\gamma$ 2 (plasmid)	Oscar Vadas	pOP737	GBB1/GG2 Sf9 expression vector (available from Burke lab)
Recombinant DNA reagent	pACEBac1-p110 $\gamma$ (144-1102) (plasmid)	This paper	MR7	PIK3CG Sf9 expression vector (available from Burke lab)
Sequence-based reagent	Fwd primer for R1021C mutation	Sigma Aldrich	PCR primers	GGCTTATCTAGCCCTTTGTCATCACAAACCTACTGATCATCCTGTTCC
Sequence-based reagent	Rev primer for R1021C mutation	Sigma Aldrich	PCR primers	AAGGGCTAGATAAGCC TTAACACAGATG
Sequence-based reagent	Fwd primer for R1021P mutation	Sigma Aldrich	PCR primers	CCTTCCTCATCACACAAACC TACTGATCATCCTGTTCTCC
Sequence-based reagent	Rev primer for R1021P mutation	Sigma Aldrich	PCR primers	GATGAGGAAGGGCTAGATAA GCCTTAACACAGATGTCCTG
Commercial assay or kit	Transcreener ADP2 FI assay (1,000 Assay, 384 Well)	BellBrook Labs	3013-1K	Lipid Kinase activity assay kit
Chemical compound, drug	GTP $\gamma$ S	Sigma Aldrich	G8634	GTP $\gamma$ S for HRas loading
Chemical compound, drug	D <sub>2</sub> O	Sigma Aldrich	151882	Heavy water for HDX
Chemical compound, drug	L- $\alpha$ -Phosphatidylcholine	Avanti	840051C	
Chemical compound, drug	L- $\alpha$ -Phosphatidylethanolamine	Sigma Aldrich	P6386	
Chemical compound, drug	L- $\alpha$ -Phosphatidylserine	Avanti	840032C	
Chemical compound, drug	L- $\alpha$ -phosphatidylinositol-4,5-bisphosphate	Avanti	840046X	

Continued on next page

Continued

Reagent type (species) or resource	Designation	Source or reference	Identifiers	Additional information
Chemical compound, drug	diC8 phosphatidylinositol-4,5-bisphosphate	Echelon Biosciences	P-4508	
Chemical compound, drug	Cholesterol	Sigma Aldrich	47127 U	
Chemical compound, drug	Sphingomyelin	Sigma Aldrich	S0756	
Chemical compound, drug	IPI-549	Chemie Tex	CT-IPI549	PMID:27660692
Chemical compound, drug	PIK-90	Axon Medchem	Axon1362	PMID:19318683
Chemical compound, drug	AS-604850	Sigma Aldrich	528108	PMID:16127437
Chemical compound, drug	Gedatolisib PF-05212384 PKI587	Bionet	FE-0013	PMID:20166697
Chemical compound, drug	Omipalisib (GSK2126458, GSK458)	LuBio Science	S2658	PMID:24900173
Chemical compound, drug	NVS-PI3-4	Haoyuan Chemexpress	HY-133907	PMID:22863202
Chemical compound, drug	AZ2	Haoyuan Chemexpress	HY-111570	PMID:30718815
Software, algorithm	HDEaminer	Sierra Analytics	<a href="http://massspec.com/hdexaminer">http://massspec.com/hdexaminer</a>	
Software, algorithm	GraphPad Prism 7	GraphPad	<a href="https://www.graphpad.com/scientific-software/prism/">https://www.graphpad.com/scientific-software/prism/</a>	
Software, algorithm	PyMOL	Schroedinger	<a href="http://pymol.org">http://pymol.org</a>	

### Expression and purification of PI3K $\gamma$ constructs

Full-length monomeric p110 $\gamma$  (WT, R1021C) and p110 $\gamma$ /p101 complex (WT, R1021C, R1021P) were expressed in Sf9 insect cells using the baculovirus expression system. For the complex, the subunits were co-expressed from a MultiBac vector (Berger *et al.*, 2004). Following 55 hr of expression, cells were harvested by centrifuging at 1680 RCF (Eppendorf Centrifuge 5810 R) and the pellets were snap-frozen in liquid nitrogen. Both the monomer and the complex were purified identically through a combination of nickel affinity, streptavidin affinity and size exclusion chromatographic techniques.

Frozen insect cell pellets were resuspended in lysis buffer (20 mM Tris pH 8.0, 100 mM NaCl, 10 mM imidazole pH 8.0, 5% glycerol [v/v], 2 mM beta-mercaptoethanol [ $\beta$ ME], protease inhibitor [Protease Inhibitor Cocktail Set III, Sigma]) and sonicated for 2 min (15 s on, 15 s off, level 4.0, Misonix sonicator 3000). Triton-X was added to the lysate to a final concentration of 0.1% and clarified by spinning at 15,000 g for 45 min (Beckman Coulter JA-20 rotor). The supernatant was loaded onto a 5 mL HisTrap FF crude column (GE Healthcare) equilibrated in NiNTA A buffer (20 mM Tris pH 8.0, 100 mM NaCl, 20 mM imidazole pH 8.0, 5% [v/v] glycerol, 2 mM  $\beta$ ME). The column was washed with high-salt NiNTA A buffer (20 mM Tris pH 8.0, 1 M NaCl, 20 mM imidazole pH 8.0, 5% [v/v] glycerol, 2 mM  $\beta$ ME), NiNTA A buffer, 6% NiNTA B buffer (20 mM Tris pH 8.0, 100 mM NaCl, 250 mM imidazole pH 8.0, 5% [v/v] glycerol, 2 mM  $\beta$ ME) and the protein was eluted with 100% NiNTA B. The eluent was loaded onto a 5 mL StrepTrap HP column (GE Healthcare) equilibrated in gel filtration buffer (20 mM Tris pH 8.5, 100 mM NaCl, 50 mM Ammonium Sulfate and 0.5 mM tris(2-carboxyethyl) phosphine [TCEP]). The column was washed with the same buffer and loaded with tobacco etch virus protease. After cleavage on the column overnight, the protein was eluted in gel filtration buffer. The eluent was concentrated in a 50,000 MWCO Amicon Concentrator (Millipore) to <1 mL and injected onto a Superdex 200 10/300 GL Increase size-exclusion column (GE Healthcare) equilibrated in gel filtration buffer. After size exclusion, the protein was concentrated, aliquoted, frozen, and stored at  $-80^{\circ}\text{C}$ .

For crystallography, p110 $\gamma$  (144–1102) was expressed in Sf9 insect cells for 72 hr. The cell pellet was lysed, and the lysate was subjected to nickel affinity purification as described above. The eluent was loaded onto HiTrap Heparin HP cation exchange column equilibrated in Hep A buffer (20 mM Tris pH 8.0, 100 mM NaCl, 5% glycerol and 2 mM  $\beta$ ME). A gradient was started with Hep B buffer (20 mM Tris pH 8.0, 1 M NaCl, 5% glycerol and 2 mM  $\beta$ ME) and the fractions containing the peak were pooled. This was then loaded onto HiTrap Q HP anion exchange column equilibrated with Hep A and again subjected to a gradient with Hep B. The peak fractions were pooled, concentrated on a 50,000 MWCO Amicon Concentrator (Millipore) to <1 mL and injected onto a Superdex 200 10/300 GL Increase size-exclusion column (GE Healthcare) equilibrated in gel filtration buffer (20 mM Tris pH 7.2, 0.5 mM (NH<sub>4</sub>)<sub>2</sub>SO<sub>4</sub>, 1% ethylene glycol, 0.02% CHAPS, and 5 mM DTT). Protein from size exclusion was concentrated to >5 mg/mL, aliquoted, frozen and stored at  $-80^{\circ}\text{C}$ .

### Expression and purification of lipidated G $\beta\gamma$

Full-length, lipidated G $\beta\gamma$  was expressed in Sf9 insect cells and purified as described previously (Kozasa, 2004). After 65 hr of expression, cells were harvested and the pellets were frozen as described above. Pellets were resuspended in lysis buffer (20 mM HEPES pH 7.7, 100 mM NaCl, 10 mM  $\beta$ ME, protease inhibitor [Protease Inhibitor Cocktail Set III, Sigma]) and sonicated for 2 min (15 s on, 15 s off, level 4.0, Misonix sonicator 3000). The lysate was spun at 500 RCF (Eppendorf Centrifuge 5810 R) to remove intact cells and the supernatant was centrifuged again at 25,000 g for 1 hr (Beckman Coulter JA-20 rotor). The pellet was resuspended in lysis buffer and sodium cholate was added to a final concentration of 1% and stirred at  $4^{\circ}\text{C}$  for 1 hr. The membrane extract was clarified by spinning at 10,000 g for 30 min (Beckman Coulter JA-20 rotor). The supernatant was diluted three times with NiNTA A buffer (20 mM HEPES pH 7.7, 100 mM NaCl, 10 mM Imidazole, 0.1% C12E10, 10 mM  $\beta$ ME) and loaded onto a 5 mL HisTrap FF crude column (GE Healthcare) equilibrated in the same buffer. The column was washed with NiNTA A, 6% NiNTA B buffer (20 mM HEPES pH 7.7, 25 mM NaCl, 250 mM imidazole pH 8.0, 0.1% C12E10, 10 mM  $\beta$ ME) and the protein was eluted with 100% NiNTA B. The eluent was loaded onto HiTrap Q HP anion exchange column equilibrated in Hep A buffer (20 mM Tris pH 8.0, 8 mM CHAPS, 2 mM Dithiothreitol [DTT]). A gradient was started with Hep B buffer (20 mM Tris pH 8.0, 500 mM NaCl, 8 mM CHAPS, 2 mM DTT) and the protein was eluted in  $\sim$ 50% Hep B buffer. The eluent was concentrated in a 30,000 MWCO Amicon Concentrator (Millipore) to <1 mL and injected onto a Superdex 75 10/300 GL size exclusion column (GE Healthcare) equilibrated in Gel Filtration buffer (20 mM HEPES pH 7.7, 100 mM NaCl, 10 mM CHAPS, 2 mM TCEP). Fractions containing protein were pooled, concentrated, aliquoted, frozen and stored at  $-80^{\circ}\text{C}$ .

### Expression and purification of lipidated HRas G12V

Full-length HRas G12V was expressed by infecting 500 mL of Sf9 cells with 5 mL of baculovirus. Cells were harvested after 55 hr of infection and frozen as described above. The frozen cell pellet was resuspended in lysis buffer (50 mM HEPES pH 7.5, 100 mM NaCl, 10 mM  $\beta$ ME and protease inhibitor (Protease Inhibitor Cocktail Set III, Sigma)) and sonicated on ice for 1 min 30 s (15 s ON, 15 s OFF, power level 4.0) on the Misonix sonicator 3000. Triton-X 114 was added to the lysate to a final concentration of 1%, mixed for 10 min at  $4^{\circ}\text{C}$  and centrifuged at 25,000 rpm for 45 min (Beckman Ti-45 rotor). The supernatant was warmed to  $37^{\circ}\text{C}$  for few minutes until it turned cloudy following which it was centrifuged at 11,000 rpm at room temperature for 10 min (Beckman JA-20 rotor) to separate the soluble and detergent-enriched phases. The soluble phase was removed, and Triton-X 114 was added to the detergent-enriched phase to a final concentration of 1%. Phase separation was performed three times. Imidazole pH 8.0 was added to the detergent phase to a final concentration of 15 mM and the mixture was incubated with Ni-NTA agarose beads (Qiagen) for 1 hr at  $4^{\circ}\text{C}$ . The beads were washed with five column volumes of Ras-NiNTA buffer A (20 mM Tris pH 8.0, 100 mM NaCl, 15 mM imidazole pH 8.0, 10 mM  $\beta$ ME and 0.5% Sodium Cholate) and the protein was eluted with two column volumes of Ras-NiNTA buffer B (20 mM Tris pH 8.0, 100 mM NaCl, 250 mM imidazole pH 8.0, 10 mM  $\beta$ ME and 0.5% Sodium Cholate). The protein was buffer exchanged to Ras-NiNTA buffer A using a 10,000 kDa MWCO Amicon concentrator, where protein was concentrated to  $\sim$ 1 mL and topped up to 15 mL with Ras-NiNTA buffer A and this was repeated a total of three times. GTP $\gamma$ S was added in twofold molar excess relative to HRas along with 25 mM EDTA. After



incubating for an hour at room temperature, the protein was buffer exchanged with phosphatase buffer (32 mM Tris pH 8.0, 200 mM Ammonium Sulphate, 0.1 mM ZnCl<sub>2</sub>, 10 mM βME and 0.5% Sodium Cholate). One unit of immobilised calf alkaline phosphatase (Sigma) was added per milligram of HRas along with twofold excess nucleotide and the mixture was incubated for 1 hr on ice. MgCl<sub>2</sub> was added to a final concentration of 30 mM to lock the bound nucleotide. The immobilised phosphatase was removed using a 0.22-micron spin filter (EMD Millipore). The protein was concentrated to less than 1 mL and was injected onto a Superdex 75 10/300 GL size exclusion column (GE Healthcare) equilibrated in gel filtration buffer (20 mM HEPES pH 7.7, 100 mM NaCl, 10 mM CHAPS, 1 mM MgCl<sub>2</sub> and 2 mM TCEP). The protein was concentrated to 1 mg/mL using a 10,000 kDa MWCO Amicon concentrator, aliquoted, snap-frozen in liquid nitrogen and stored at −80°C.

### Lipid vesicle preparation

For kinase assays comparing WT and mutant activities, lipid vesicles containing 5% brain phosphatidylinositol 4,5- biphosphate (PIP<sub>2</sub>), 20% brain phosphatidylserine (PS), 50% egg-yolk phosphatidylethanolamine (PE), 10% egg-yolk phosphatidylcholine (PC), 10% cholesterol and 5% egg-yolk sphingomyelin (SM) were prepared by mixing the lipids dissolved in organic solvent. The solvent was evaporated in a stream of argon following which the lipid film was desiccated in a vacuum for 45 min. The lipids were resuspended in lipid buffer (20 mM HEPES pH 7.0, 100 mM NaCl and 10% glycerol) and the solution was sonicated for 15 min. The vesicles were subjected to five freeze thaw cycles and extruded 11 times through a 100 nm filter (T and T Scientific: TT-002–0010). The extruded vesicles were sonicated again for 5 min, aliquoted and stored at −80°C. For inhibitor response assays, lipid vesicles containing 95% PS and 5% C8-PIP<sub>2</sub> were used. PS was dried and desiccated as described above. The lipid film was mixed and resuspended with C8-PIP<sub>2</sub> solution (2.5 mg/mL in lipid buffer). Following this, vesicles were essentially prepared the same way as described above. All vesicles were stored at 5 mg/mL.

### Lipid kinase assays

All lipid kinase activity assays employed the Transcreeper ADP2 Fluorescence Intensity (FI) Assay (Bellbrook labs) which measures ADP production. For assays comparing the activities of mutants, final concentrations of PM-mimic vesicles were 1 mg/mL, ATP was 100 μM and lipidated Gβγ/HRas were at 1.5 μM. Two μL of a PI3K solution at 2X final concentration (50–3000 nM final) was mixed with 2 μL substrate solution containing ATP, vesicles and Gβγ/HRas or Gβγ/HRas gel filtration buffer and the reaction was allowed to proceed for 60 min at 20°C. The reaction was stopped with 4 μL of 2X stop and detect solution containing Stop and Detect buffer, 8 nM ADP Alexa Fluor 594 Tracer and 93.7 μg/mL ADP2 Antibody IRDye QC-1 and incubated for 50 min. The fluorescence intensity was measured using a SpectraMax M5 plate reader at excitation 590 nm and emission 620 nm. This data was normalised against a 0–100% ADP window made using conditions containing either 100 μM ATP/ADP with vesicles and kinase buffer. % ATP turnover was interpolated from an ATP standard curve obtained from performing the assay on 100 μM (total) ATP/ADP mixtures with increasing concentrations of ADP using Prism 7. All specific activities of lipid kinase activity were corrected for the basal ATPase activity by subtracting the specific activity of the WT/mutant protein in the absence of vesicles/activators.

For assays measuring inhibitor response, substrate solutions containing vesicles, ATP and Gβγ at 4X final concentration (as described above) were mixed with 4X solutions of inhibitor dissolved in lipid buffer (<1% DMSO) in serial to obtain 2X substrate solutions with inhibitors at the various 2X concentrations. Two μL of this solution was mixed with 2 μL of 2X protein solution (4 nM final for the mutant and 8 nM final for WT) to start the reaction and allowed to proceed for 60 min at 37°C. Following this, the reaction was stopped and the intensity was measured. The raw data was normalised against a 0–100% ADP window as described above. The % inhibition was calculated by comparison to the activity with no inhibitor to obtain fraction activity remaining.

### Hydrogen deuterium exchange mass spectrometry (HDX-MS)

HDX experiments were performed similarly as described before (*Dornan et al., 2017*). For HDX with mutants, 3 μL containing 13 picomoles of protein was incubated with 8.25 μL of D<sub>2</sub>O buffer (20 mM HEPES pH 7.5, 100 mM NaCl, 98% (v/v) D<sub>2</sub>O) for four different time periods (3, 30, 300, 3000 s at

20°C). After the appropriate time, the reaction was stopped with 57.5  $\mu\text{L}$  of ice-cold quench buffer (2M guanidine, 3% formic acid), immediately snap frozen in liquid nitrogen and stored at  $-80^\circ\text{C}$ . For HDX with inhibitors, 5  $\mu\text{L}$  of p110 $\gamma$  or p110 $\gamma$ /p101 at 2  $\mu\text{M}$  was mixed with 5  $\mu\text{L}$  of inhibitor at 4  $\mu\text{M}$  in 10% DMSO or 5  $\mu\text{L}$  of blank solution containing 10% DMSO and incubated for 20 min on ice. A total of 40  $\mu\text{L}$  of D<sub>2</sub>O buffer was added to this solution to start the exchange reaction which was allowed to proceed for four different time periods (3, 30, 300, 3000 s at 20°C). After the appropriate time, the reaction was terminated with 20  $\mu\text{L}$  of ice-cold quench buffer and the samples were frozen.

Protein samples were rapidly thawed and injected onto an ultra-high-pressure liquid chromatography (UPLC) system at 2°C. Protein was run over two immobilised pepsin columns (Trajan, ProDx protease column, PDX.PP01-F32 and Applied Biosystems, Porosyme, 2-3131-00) at 10°C and 2°C at 200  $\mu\text{L}/\text{min}$  for 3 min, and peptides were collected onto a VanGuard precolumn trap (Waters). The trap was subsequently eluted in line with an Acquity 1.7  $\mu\text{m}$  particle,  $100 \times 1 \text{ mm}^2$  C18 UPLC column (Waters), using a gradient of 5–36% B (buffer A, 0.1% formic acid; buffer B, 100% acetonitrile) over 16 min. Mass spectrometry experiments were performed on an Impact II TOF (Bruker) acquiring over a mass range from 150 to 2200 m/z using an electrospray ionisation source operated at a temperature of 200°C and a spray voltage of 4.5 kV. Peptides were identified using data-dependent acquisition methods following tandem MS/MS experiments (0.5 s precursor scan from 150 to 2000 m/z; 12 0.25 s fragment scans from 150 to 2000 m/z). MS/MS datasets were analysed using PEAKS7 (PEAKS), and a false discovery rate was set at 1% using a database of purified proteins and known contaminants.

HD-Examiner software (Sierra Analytics) was used to automatically calculate the level of deuterium incorporation into each peptide. All peptides were manually inspected for correct charge state and presence of overlapping peptides. Deuteration levels were calculated using the centroid of the experimental isotope clusters. The results for these proteins are presented as the raw percent deuterium incorporation, as shown in Supplemental Data, with the only correction being applied correcting for the deuterium oxide percentage of the buffer utilised in the exchange (62% for experiments with mutants and 75.5% for experiments with inhibitors). No corrections for back exchange that occurs during the quench and digest/separation were applied. Attempts to generate a fully deuterated class I PI3K sample were unsuccessful, which is common for large macromolecular complexes. Therefore, all deuterium exchange values are relative.

Changes in any peptide at any time point greater than both 5% and 0.4 Da between conditions with a paired t test value of  $p < 0.01$  were considered significant. Peptides that crossed these criteria were mapped onto the structures in **Figure 2A+B** and **Figure 4B-D**. Peptides that crossed this threshold are annotated on the raw HDX data in the source data excel file according to the legend. The raw HDX data are shown in two different formats. The raw peptide deuterium incorporation graphs for a selection of peptides with significant differences are shown, with the raw data for all analysed peptides in the source data. To allow for visualisation of differences across all peptides, we utilised number of deuterium difference (#D) plots. These plots show the total difference in deuterium incorporation over the entire H/D exchange time course, with each point indicating a single peptide. These graphs are calculated by summing the differences at every time point for each peptide and propagating the error (example **Figure 2C–F**). This visualisation was utilised over the similar strategy of graphing differences at each timepoint separately as it allowed for the display of multiple comparisons on the same graph (example **Figure 4A**).

The mass spectrometry proteomics data have been deposited to the ProteomeXchange Consortium via the PRIDE partner repository (*Perez-Riverol et al., 2019*) with the dataset identifier PXD021132.

### X-ray crystallography:

p110 $\gamma$  (144–1102) was crystallised from a grid of 2  $\mu\text{L}$  sitting drops at 1:1, 2:1 and 3:1 protein to reservoir ratios at 18°C. Protein at 4 mg/mL (in 20 mM Tris pH 7.2, 0.5 mM  $(\text{NH}_4)_2\text{SO}_4$ , 1% ethylene glycol, 0.02% CHAPS and 5 mM DTT) was mixed with reservoir solution containing 100 mM Tris pH 7.5, 250 mM  $(\text{NH}_4)_2\text{SO}_4$  and 20–22% PEG 4000. Large multinucleate crystals were generated in these drops. Inhibitor stocks were prepared at concentrations of 0.01 mM, 0.1 mM and 1 mM in cryo-protectant solution containing 100 mM Tris pH 7.5, 250 mM  $(\text{NH}_4)_2\text{SO}_4$ , 23% PEG 4000% and 14% glycerol. Inhibitors at increasing concentrations were added to the drops stepwise every 1 hr. After overnight incubation with the inhibitor, single crystals were manually broken from the multi-nucleates

and soaked in a fresh drop containing 1 mM inhibitor in cryo-protectant before being immediately frozen in liquid nitrogen. The final crystals were rod/needle shaped and had dimensions of roughly  $10 \times 20 \times 80 \mu\text{m}$ , and were mounted on either 0.1–0.2 or 0.05–0.1 mm cryo loops (Hampton Research). Each unique structure of PI3K bound to inhibitors was solved from a single crystal.

Diffraction data for PI3K $\gamma$  crystals were collected on beamline 08ID-1 of the Canadian Light Source. Data was collected at 0.97949 Å using a beam width of 50  $\mu\text{m}$ . Diffraction data for each unique crystal was collected using a strategy of 0.2–0.4 s exposure/0.2° rotation for each image, over a total rotational range of 180°. Data were processed using XDS (Kabsch, 2010). Phases were initially obtained by molecular replacement using Phaser (McCoy et al., 2007) using PDB: 2CHW for the IPI-549 complex (Knight et al., 2006), and 5JHA for Gedatolisib and NVS-PI3-4 (Bohnacker et al., 2017). Iterative model building and refinement were performed in COOT (Emsley et al., 2010) and phenix.refine (Afonine et al., 2012). Refinement was carried out with rigid body refinement, followed by translation/libration/screw B-factor and xyz refinement, with the final round of refinement optimising X-ray/stereochemistry and X-ray/ADP weighting. The final model was verified in Molprobity (Chen et al., 2010) to examine all Ramachandran and Rotamer outliers. Data collection and refinement statistics are shown in **Supplementary file 6**. The crystallography data has been deposited in the protein data bank with accession numbers (PDB: 7JWE, 7J × 0, 7JWZ).

### Molecular dynamics: missing loops modelling

The employed crystallographic structures of the p110 $\gamma$  protein reveal several missing gaps corresponding to flexible loops within range of the ligand-binding site: the activation loop (residues 968–981), and loops connecting the C2 and helical domains (residues 435–460 and 489–497). These missing gaps were modelled as disordered loops using Modeller9.19 (Sali and Blundell, 1993). Keeping the crystallographic coordinates fixed, 50 models were independently generated for each system. The wild type (WT), R1021C, and R1021P systems used PDB ID 6AUD (Safina et al., 2017) with their corresponding mutations in the mutant systems. The alignment used by Modeller between the crystallographic structure sequences and the FASTA sequence of p110 $\gamma$  (Uniprot ID P48736) were generated using Clustal Omega (Sievers et al., 2011). The top models were visually inspected to discard those in which loops were entangled in a knot or clashed with the rest of the structure. Lastly, from the remaining models, three were selected for each system to initiate simulations in triplicates.

### Molecular dynamics: system preparation

The generated models were prepared using tleap program of the AMBER package (Case et al., 2005). The systems were parametrised using the general AMBER force field (GAFF) using ff14sb for the protein (Maier et al., 2015). The systems were fully solvated with explicit water molecules described using the TIP3P model (Jorgensen et al., 1983), adding K<sup>+</sup> and Cl<sup>-</sup> counterions to neutralise the total charge. The total number of atoms is 97,861 for WT (size: 116 Å × 95 Å × 94 Å), 100,079 for R1021C (size: 116 Å × 95 Å × 94 Å), 97,861 for R1021P (size: 116 Å × 95 Å × 94 Å).

### Gaussian accelerated molecular dynamics (GaMD)

All-atom MD simulations were conducted using the GPU version of AMBER18 (Case et al., 2005). The systems were initially relaxed through a series of minimisation, heating, and equilibration cycles. During the first cycle, the protein was restrained using a harmonic potential with a force constant of 10 kcal/mol-Å<sup>2</sup>, while the solvent, and ions were subjected to an initial minimisation of 2000 steps using the steepest descent approach for 1000 steps and conjugate gradient approach for another 1000 steps. The full system (protein + solvent) was then similarly minimised for 1000 and 4000 steps using the steepest descent and conjugate gradient approaches, respectively. Subsequently, the temperature was incrementally changed from 100 to 300 K for 10 ps at two fs/step (NVT ensemble). Next, the systems were equilibrated for 200 ps at 1 atm and 300K (NPT ensemble), and for 200ps at 300K (NVT ensemble). Lastly, more equilibration simulations were run in the NVT ensemble in two steps; all systems were simulated using conventional MD for 50 ns and GaMD for 50ns. Temperature control (300 K) and pressure control (one atm) were performed via Langevin dynamics and Berendsen barostat, respectively. Production GaMD were simulated for ~3  $\mu\text{s}$  for WT, ~4.1  $\mu\text{s}$  R1021C, ~1.5  $\mu\text{s}$  for R1021P. GaMD is an unconstrained enhanced sampling approach that works by adding a

harmonic boost potential to smooth biomolecular potential energy surface and reduce the system energy barriers (Miao et al., 2015). Details of the GaMD method have been extensively described in previous studies (Miao et al., 2015; Pang et al., 2017).

### GaMD analysis: principal component analysis (PCA)

PCA was performed using the `sklearn.decomposition.PCA` function in the *Scikit-learn* library using python3.6.9. First, all simulations were aligned with *mdtraj* (McGibbon et al., 2015) onto the same initial coordinates using C $\alpha$  atoms of the kinase domain (residues 726–1088). Next, simulation coordinates of each domain of interest (for example  $\kappa 9$ - $\kappa 10$ ) from all systems (WT, R1021C, and R1021P) and replicas were concatenated and used to fit the transformation function. Subsequently, the fitted transformation function was applied to reduce the dimensionality of each domain's simulation C $\alpha$  coordinates. It is important to note that all systems are transformed into the same PC space to evaluate the simulation variance across systems.

### GaMD analysis: angles calculation

Inter-helical angles were calculated using in-house python scripts along with *mdtraj* (McGibbon et al., 2015) as the angle between two vectors representing the principal axis along each helix. Each principal axis connects two points corresponding to the center of mass (COM) of the first and last turn from each helix. For  $\kappa 8$ , points 1 and 2 are represented by the COM of residues 1020–1023 and 1004–1007 C $\alpha$  coordinates, respectively. For  $\kappa 9$ , points 1 and 2 are represented by the COM of residues 1024–1027 and 1034–1037 C $\alpha$  coordinates, respectively. For  $\kappa 10$ , points 1 and 2 are represented by the COM of residues 1053–1056 and 1046–1049 C $\alpha$  coordinates, respectively. For  $\kappa 11$ , points 1 and 2 are represented by the COM of residues 1062–1065 and 1074–1077 C $\alpha$  coordinates, respectively. Angles were computed at each frame along the trajectories after structural alignment onto the initial coordinates using the C $\alpha$  atoms of the kinase domain (residues 726–1088) as a reference.

### GaMD analysis: hydrogen bonds calculation

Hydrogen bonds were calculated using the *baker hubbard* command implemented with *mdtraj* (McGibbon et al., 2015). Occupancy (%) was determined by counting the number of frames in which a specific hydrogen bond was formed with respect to the total number of frames and then averaged across replicas.

### GaMD analysis: root-mean-square-fluctuations (RMSF)

RMSF was calculated using in-house python scripts along with *mdtraj* (McGibbon et al., 2015). RMSF was computed for each residue atom and represented as box plot to show the range of RMSF values across replicas. The trajectories were aligned onto the initial coordinates using the C $\alpha$  atoms of the kinase domain (residues 726–1088) as a reference.

### PI3K inhibitors

Compounds were purchased from companies indicated below in  $\geq 95\%$  purity (typical 98% pure). IPI-549 (Evans et al., 2016) was purchased from ChemieTex (Indianapolis, USA, #CT-IPI549); PIK-90 (Knight et al., 2006) from Axon Medchem (Groningen, The Netherlands, #Axon1362); AS-604850 (PI 3-Ky Inhibitor II, Calbiochem) (Camps et al., 2005) from Sigma Aldrich (#528108); Gedatolisib (PF-05212384, PKI587) (Venkatesan et al., 2010) from Bionet (Camelford, UK, #FE-0013); Omipalisib (GSK2126458, GSK458) (Knight et al., 2010) from LuBioScience GmbH (Zurich, Switzerland, #S2658); NVS-PI3-4 (Collmann et al., 2013; Bruce et al., 2012) and AZg1 (AZ2) (Gangadhara et al., 2019) from Haoyuan Chemexpress Co., Ltd. (Shanghai, China, #HY-133907 and #HY-111570, respectively).

### Acknowledgements

JEB is supported by a new investigator grant from the Canadian Institute of Health Research (CIHR), a Michael Smith Foundation for Health Research (MSFHR) Scholar award (17686), and an operating grant from the Cancer Research Society (CRS-24368). REA and ZG are supported in part by NIH



GM132826 and NCI P01-CA234228. MPW is funded by the Stiftung für Krebsbekämpfung grant 341, the Swiss National Science Foundation grant 310030\_189065, the Novartis Foundation for medical-biological Research grant 14B095; and the Innosuisse grant 37213.1 IP-LS. We appreciate feedback from members of the Burke lab during preparation.

---

## Additional information

### Funding

Funder	Grant reference number	Author
Cancer Research Society	CRS-24368	John E Burke
Michael Smith Foundation for Health Research	17686	John E Burke
Canadian Institutes of Health Research	New Investigator	John E Burke
National Institutes of Health	GM132826	Zied Gaieb Rommie E Amaro
Stiftung FHNW	341	Matthias P Wymann
Swiss National Science Foundation	310030_189065	Matthias P Wymann
Novartis Foundation	14B095	Matthias P Wymann
Innosuisse - Schweizerische Agentur für Innovationsförderung	37213.1 IP-LS	Matthias P Wymann
National Cancer Institute	P01-CA234228	Zied Gaieb Rommie E Amaro

The funders had no role in study design, data collection and interpretation, or the decision to submit the work for publication.

### Author contributions

Manoj K Rathinaswamy, Conceptualization, Formal analysis, Investigation, Methodology, Writing - original draft, Writing - review and editing; Zied Gaieb, Software, Formal analysis, Validation, Investigation, Methodology, Writing - review and editing; Kaelin D Fleming, Data curation, Software, Formal analysis, Validation, Methodology, Writing - review and editing; Chiara Borsari, Resources, Investigation, Writing - review and editing; Noah J Harris, Investigation, Methodology, Writing - review and editing; Brandon E Moeller, Software, Methodology; Matthias P Wymann, Supervision, Funding acquisition, Validation, Writing - original draft, Writing - review and editing; Rommie E Amaro, Supervision, Funding acquisition, Methodology, Writing - review and editing; John E Burke, Conceptualization, Formal analysis, Supervision, Funding acquisition, Methodology, Writing - original draft, Project administration, Writing - review and editing

### Author ORCIDs

Manoj K Rathinaswamy  <https://orcid.org/0000-0001-5909-4353>

Chiara Borsari  <http://orcid.org/0000-0002-4688-8362>

Matthias P Wymann  <http://orcid.org/0000-0003-3349-4281>

John E Burke  <https://orcid.org/0000-0001-7904-9859>

### Decision letter and Author response

Decision letter <https://doi.org/10.7554/eLife.64691.sa1>

Author response <https://doi.org/10.7554/eLife.64691.sa2>

## Additional files

### Supplementary files

- Supplementary file 1. HDX-MS experimental conditions and data analysis parameters for **Figure 2** from the guidelines of the IC-HDX-MS community (*Masson et al., 2019*).
- Supplementary file 2. HDX-MS experimental conditions and data analysis parameters for **Figure 4** from the guidelines of the IC-HDX-MS community (*Masson et al., 2019*).
- Supplementary file 3. HDX-MS experimental conditions and data analysis parameters for **Figure 2—figure supplement 1** from the guidelines of the IC-HDX-MS community (*Masson et al., 2019*).
- Supplementary file 4. HDX-MS experimental conditions and data analysis parameters for **Figure 4—figure supplement 1** from the guidelines of the IC-HDX-MS community (*Masson et al., 2019*).
- Supplementary file 5. List of all PI3K inhibitors analysed in this manuscript. IC<sub>50</sub>s for class IA and IB are listed from the reference attached. N.D. is not determined.
- Supplementary file 6. X-ray crystallography collection and refinement statistics.
- Transparent reporting form

### Data availability

The crystallography data has been deposited in the protein data bank with accession numbers (PDB: 7JWE, 7JX0, 7JWZ). The mass spectrometry proteomics data have been deposited to the ProteomeXchange Consortium via the PRIDE partner repository with the dataset identifier PXD021132. All data generated or analyzed during this study are included in the manuscript and supporting files. Specifically biochemical kinase assay data are included in the source data files.

The following datasets were generated:

Author(s)	Year	Dataset title	Dataset URL	Database and Identifier
Rathinaswamy MK, Gaieb Z, Fleming KD, Borsari C, Harris NJ, Moeller BE, Wymann MP, Amaro RE, Burke JE	2021	Gedatolisib bound to the PI3Kγ catalytic subunit p110 gamma	<a href="https://www.rcsb.org/structure/7JWE">https://www.rcsb.org/structure/7JWE</a>	RCSB Protein Data Bank, 7JWE
Rathinaswamy MK, Gaieb Z, Fleming KD, Borsari C, Harris NJ, Moeller BE, Wymann MP, Amaro RE, Burke JE	2021	NVS-PI3-4 bound to the PI3Kγ catalytic subunit p110 gamma	<a href="https://www.rcsb.org/structure/7JX0">https://www.rcsb.org/structure/7JX0</a>	RCSB Protein Data Bank, 7JX0
Rathinaswamy MK, Gaieb Z, Fleming KD, Borsari C, Harris NJ, Moeller BE, Wymann MP, Amaro RE, Burke JE	2021	IPI-549 bound to the PI3Kγ catalytic subunit p110 gamma	<a href="https://www.rcsb.org/structure/7JWZ">https://www.rcsb.org/structure/7JWZ</a>	RCSB Protein Data Bank, 7JWZ
Rathinaswamy MK, Gaieb Z, Fleming KD, Borsari C, Harris NJ, Moeller BE, Wymann MP, Amaro RE, Burke JE	2021	Targeting of disease-linked mutations in PI3K gamma	<a href="https://www.ebi.ac.uk/pride/archive/projects/PXD021132">https://www.ebi.ac.uk/pride/archive/projects/PXD021132</a>	PRIDE, PXD021132

The following previously published datasets were used:

Author(s)	Year	Dataset title	Dataset URL	Database and Identifier
Tate JG, Bamford S, Jubb HC,	2019	COSMIC: the Catalogue Of Somatic Mutations In Cancer	<a href="https://cancer.sanger.ac.uk/cosmic">https://cancer.sanger.ac.uk/cosmic</a>	COSMIC, COSMIC

Sondka Z, Beare DM, Bindal N, Boutselakis H, Cole CG, Creatore C, Dawson E, Fish P, Harsha B, Hathaway C, Jupe SC, Kok CY, Noble K, Ponting L, Ramshaw CC, Rye CE, Speedy HE, Stefancsik R, Thompson SL, Wang S, Ward S, Campbell PJ, Forbes SA

Murray JM, Ultsch M	2017	PI3K-gamma K802T in complex with Cpd 8 10-((1-(tert-butyl)piperidin-4-yl)sulfinyl)-2-(1-isopropyl-1H-1,2,4-triazol-5-yl)-5,6-dihydrobenzo[f]imidazo[1,2-d][1,4]oxazepine	<a href="https://www.rcsb.org/structure/6AUD">https://www.rcsb.org/structure/6AUD</a>	RCSB Protein Data Bank, 6AUD
Knight ZA, Gonzalez B, Feldman ME, Zunder ER, Goldenberg DD, Williams O, Loewith R, Stokoe D, Balla A, Toth B, Balla T, Weiss WA, Williams RL, Shokat KM	2006	A pharmacological map of the PI3-K family defines a role for p110alpha in signaling: The structure of complex of phosphoinositide 3-kinase gamma with inhibitor PIK-90	<a href="https://www.rcsb.org/structure/2CHX">https://www.rcsb.org/structure/2CHX</a>	RCSB Protein Data Bank, 2CHX
Camps M, Ruckle T, Ji H, Ardisson V, Rintelen F, Shaw J, Ferrandi C, Chabert C, Gillieron C, Francon B, Martin T, Gretener D, Perrin D, Leroy D, Vitte P-A, Hirsch E, Wymann MP, Cirillo R, Schwarz MK, Rommel C	2005	Crystal structure of human PI3Kgamma complexed with AS604850	<a href="https://www.rcsb.org/structure/2a4z">https://www.rcsb.org/structure/2a4z</a>	RCSB Protein Data Bank, 2A4Z
Elkins PA, Marrero EM	2009	Structure of Pi3K gamma with a potent inhibitor: GSK2126458	<a href="https://www.rcsb.org/structure/3L08">https://www.rcsb.org/structure/3L08</a>	RCSB Protein Data Bank, 3L08

## References

- AACR Project GENIE Consortium.** 2017. AACR project GENIE: powering precision medicine through an international consortium. *Cancer Discov. American Association for Cancer Research* **7**:818–831. DOI: <https://doi.org/10.1158/2159-8290.CD-17-0151>
- Afonine PV, Grosse-Kunstleve RW, Echols N, Headd JJ, Moriarty NW, Mustyakimov M, Terwilliger TC, Urzhumtsev A, Zwart PH, Adams PD.** 2012. Towards automated crystallographic structure refinement with phenix.refine. *Acta Crystallographica Section D Biological Crystallography* **68**:352–367. DOI: <https://doi.org/10.1107/S0907444912001308>, PMID: 22505256
- Afonine PV, Moriarty NW, Mustyakimov M, Sobolev OV, Terwilliger TC, Turk D, Urzhumtsev A, Adams PD.** 2015. FEM: feature-enhanced map. *Acta Crystallographica Section D Biological Crystallography* **71**:646–666. DOI: <https://doi.org/10.1107/S1399004714028132>, PMID: 25760612
- André F, Ciruelos E, Rubovszky G, Campone M, Loibl S, Rugo HS, Iwata H, Conte P, Mayer IA, Kaufman B, Yamashita T, Y-s L, Inoue K, Takahashi M, Pápai Z, Longin A-S, Mills D, Wilke C, Hirawat S, Juric D, SOLAR-1 Study Group.** 2019. Alpelisib for PIK3CA-Mutated, hormone Receptor-Positive advanced breast Cancer. *N Engl J Med* **380**:1929–1940. DOI: <https://doi.org/10.1056/NEJMoa1813904>
- Angulo I, Vadas O, Garcon F, Banham-Hall E, Plagnol V, Leahy TR, Baxendale H, Coulter T, Curtis J, Wu C, Blake-Palmer K, Perisic O, Smyth D, Maes M, Fiddler C, Juss J, Cilliers D, Markelj G, Chandra A, Farmer G, et al.** 2013. Phosphoinositide 3-Kinase Gene Mutation Predisposes to Respiratory Infection and Airway Damage. *Science* **342**:866–871. DOI: <https://doi.org/10.1126/science.1243292>
- Barber DF, Bartolomé A, Hernandez C, Flores JM, Redondo C, Fernandez-Arias C, Camps M, Ruckle T, Schwarz MK, Rodríguez S, Martínez-A C, Balomenos D, Rommel C, Carrera AC.** 2005. PI3Kγ inhibition blocks

- glomerulonephritis and extends lifespan in a mouse model of systemic lupus. *Nature Medicine* **11**:933–935. DOI: <https://doi.org/10.1038/nm1291>
- Barbier M**, Attoub S, Calvez R, Laffargue M, Jarry A, Mareel M, Altruda F, Gespach C, Wu D, Lu B, Hirsch E, Wymann MP. 2001. Tumour biology weakening link to colorectal cancer? *Nature Publishing Group* **413**:796. DOI: <https://doi.org/10.1038/35101660>
- Berger I**, Fitzgerald DJ, Richmond TJ. 2004. Baculovirus expression system for heterologous multiprotein complexes. *Nature Biotechnology* **22**:1583–1587. DOI: <https://doi.org/10.1038/nbt1036>
- Berndt A**, Miller S, Williams O, Le DD, Houseman BT, Pacold JI, Gorrec F, Hon W-C, Ren P, Liu Y, Rommel C, Gaillard P, Rückle T, Schwarz MK, Shokat KM, Shaw JP, Williams RL. 2010. The p110 $\delta$  structure: mechanisms for selectivity and potency of new PI(3)K inhibitors. *Nature Chemical Biology* **6**:117–124. DOI: <https://doi.org/10.1038/nchembio.293>
- Bilanges B**, Posor Y, Vanhaesebroeck B. 2019. PI3K isoforms in cell signalling and vesicle trafficking. *Nature Reviews Molecular Cell Biology* **20**:515–534. DOI: <https://doi.org/10.1038/s41580-019-0129-z>, PMID: 31110302
- Bohnacker T**, Marone R, Collmann E, Calvez R, Hirsch E, Wymann MP. 2009. PI3K $\gamma$  adaptor subunits define coupling to degranulation and cell motility by distinct PtdIns(3,4,5)P $_3$  pools in mast cells. *Science Signaling* **2**:ra27. DOI: <https://doi.org/10.1126/scisignal.2000259>, PMID: 19509406
- Bohnacker T**, Prota AE, Beauflis F, Burke JE, Melone A, Inglis AJ, Rageot D, Sele AM, Cmiljanovic V, Cmiljanovic N, Bargsten K, Aher A, Akhmanova A, Díaz JF, Fabbro D, Zvelebil M, Williams RL, Steinmetz MO, Wymann MP. 2017. Deconvolution of Buparlisib's mechanism of action defines specific PI3K and tubulin inhibitors for therapeutic intervention. *Nature Communications* **8**:14683. DOI: <https://doi.org/10.1038/ncomms14683>, PMID: 28276440
- Breasson L**, Becattini B, Sardi C, Molinaro A, Zani F, Marone R, Botindari F, Bousquenaud M, Ruegg C, Wymann MP, Solinas G. 2017. PI3K $\gamma$  activity in leukocytes promotes adipose tissue inflammation and early-onset insulin resistance during obesity. *Science Signaling* **10**:eaaf2969. DOI: <https://doi.org/10.1126/scisignal.aaf2969>, PMID: 28720716
- Brown JR**, Byrd JC, Coutre SE, Benson DM, Flinn IW, Wagner-Johnston ND, Spurgeon SE, Kahl BS, Bello C, Webb HK, Johnson DM, Peterman S, Li D, Jahn TM, Lannutti BJ, Ulrich RG, Yu AS, Miller LL, Furman RR. 2014. Idelalisib, an inhibitor of phosphatidylinositol 3-kinase p110 $\delta$ , for relapsed/refractory chronic lymphocytic leukemia. *Blood* **123**:3390–3397. DOI: <https://doi.org/10.1182/blood-2013-11-535047>, PMID: 24615777
- Bruce I**, Akhlaq M, Bloomfield GC, Budd E, Cox B, Cuenoud B, Finan P, Gedeck P, Hatto J, Hayler JF, Head D, Keller T, Kirman L, Leblanc C, Le Grand D, McCarthy C, O'Connor D, Owen C, Oza MS, Pilgrim G, et al. 2012. Development of isoform selective PI3-kinase inhibitors as pharmacological tools for elucidating the PI3K pathway. *Bioorganic & Medicinal Chemistry Letters* **22**:5445–5450. DOI: <https://doi.org/10.1016/j.bmcl.2012.07.042>, PMID: 22863202
- Burke JE**, Vadas O, Berndt A, Finegan T, Perisic O, Williams RL. 2011. Dynamics of the phosphoinositide 3-kinase p110 $\delta$  interaction with p85 $\alpha$  and membranes reveals aspects of regulation distinct from p110 $\alpha$ . *Structure* **19**:1127–1137. DOI: <https://doi.org/10.1016/j.str.2011.06.003>, PMID: 21827948
- Burke JE**, Perisic O, Masson GR, Vadas O, Williams RL. 2012. Oncogenic mutations mimic and enhance dynamic events in the natural activation of phosphoinositide 3-kinase p110 $\alpha$  (PIK3CA). *PNAS* **109**:15259–15264. DOI: <https://doi.org/10.1073/pnas.1205508109>, PMID: 22949682
- Burke JE**. 2018. Structural basis for regulation of phosphoinositide kinases and their involvement in human disease. *Molecular Cell* **71**:653–673. DOI: <https://doi.org/10.1016/j.molcel.2018.08.005>, PMID: 30193094
- Burke JE**, Williams RL. 2013. Dynamic steps in receptor tyrosine kinase mediated activation of class IA phosphoinositide 3-kinases (PI3K) captured by H/D exchange (HDX-MS). *Advances in Biological Regulation* **53**:97–110. DOI: <https://doi.org/10.1016/j.jbior.2012.09.005>, PMID: 23194976
- Campa CC**, Silva RL, Margaria JP, Pirali T, Mattos MS, Kraemer LR, Reis DC, Grosa G, Copperi F, Dalmarco EM, Lima-Júnior RCP, Aprile S, Sala V, Dal Bello F, Prado DS, Alves-Filho JC, Medana C, Cassali GD, Tron GC, Teixeira MM, et al. 2018. Inhalation of the prodrug PI3K inhibitor CL27c improves lung function in asthma and fibrosis. *Nature Communications* **9**:5232. DOI: <https://doi.org/10.1038/s41467-018-07698-6>, PMID: 30542075
- Camps M**, Rückle T, Ji H, Ardisson V, Rintelen F, Shaw J, Ferrandi C, Chabert C, Gillieron C, Françon B, Martin T, Gretener D, Perrin D, Leroy D, Vitte PA, Hirsch E, Wymann MP, Cirillo R, Schwarz MK, Rommel C. 2005. Blockade of PI3K $\gamma$  suppresses joint inflammation and damage in mouse models of rheumatoid arthritis. *Nature Medicine* **11**:936–943. DOI: <https://doi.org/10.1038/nm1284>, PMID: 16127437
- Case DA**, Cheatham TE, Darden T, Gohlke H, Luo R, Merz KM, Onufriev A, Simmerling C, Wang B, Woods RJ. 2005. The amber biomolecular simulation programs. *Journal of Computational Chemistry* **26**:1668–1688. DOI: <https://doi.org/10.1002/jcc.20290>, PMID: 16200636
- Chen VB**, Arendall WB, Headd JJ, Keedy DA, Immormino RM, Kapral GJ, Murray LW, Richardson JS, Richardson DC. 2010. MolProbity: all-atom structure validation for macromolecular crystallography. *Acta Crystallographica Section D Biological Crystallography* **66**:12–21. DOI: <https://doi.org/10.1107/S0907444909042073>, PMID: 20057044
- Collier PN**, Martinez-Botella G, Cornebise M, Cottrell KM, Doran JD, Griffith JP, Mahajan S, Maltais F, Moody CS, Huck EP, Wang T, Aronov AM. 2015. Structural basis for isoform selectivity in a class of benzothiazole inhibitors of phosphoinositide 3-kinase  $\gamma$ . *Journal of Medicinal Chemistry* **58**:517–521. DOI: <https://doi.org/10.1021/jm500362j>, PMID: 24754609
- Collmann E**, Bohnacker T, Marone R, Dawson J, Rehberg M, Stringer R, Krombach F, Burkhart C, Hirsch E, Hollingworth GJ, Thomas M, Wymann MP. 2013. Transient targeting of phosphoinositide 3-kinase acts as a

- roadblock in mast cells' route to allergy. *Journal of Allergy and Clinical Immunology* **132**:959–968. DOI: <https://doi.org/10.1016/j.jaci.2013.03.008>, PMID: 23683463
- De Henau O, Rausch M, Winkler D, Campesato LF, Liu C, Cymerman DH, Budhu S, Ghosh A, Pink M, Tchaicha J, Douglas M, Tibbitts T, Sharma S, Proctor J, Kosmider N, White K, Stern H, Soglia J, Adams J, Palombella VJ, et al. 2016. Overcoming resistance to checkpoint blockade therapy by targeting PI3K $\gamma$  in myeloid cells. *Nature* **539**:443–447. DOI: <https://doi.org/10.1038/nature20554>, PMID: 27828943
- Deladeriere A, Gambardella L, Pan D, Anderson KE, Hawkins PT, Stephens LR. 2015. The regulatory subunits of PI3K $\gamma$  control distinct neutrophil responses. *Science Signaling* **8**:ra8. DOI: <https://doi.org/10.1126/scisignal.2005564>, PMID: 25605974
- Dituri F, Mazzocca A, Lupo L, Edling CE, Azzariti A, Antonaci S, Falasca M, Giannelli G. 2012. PI3K class IB controls the cell cycle checkpoint promoting cell proliferation in hepatocellular carcinoma. *International Journal of Cancer* **130**:2505–2513. DOI: <https://doi.org/10.1002/ijc.26319>, PMID: 21796621
- Dornan GL, Siempelkamp BD, Jenkins ML, Vadas O, Lucas CL, Burke JE. 2017. Conformational disruption of PI3K $\delta$  regulation by immunodeficiency mutations in *PIK3CD* and *PIK3R1*. *PNAS* **114**:1982–1987. DOI: <https://doi.org/10.1073/pnas.1617244114>, PMID: 28167755
- Dornan GL, Burke JE. 2018. Molecular mechanisms of human disease mediated by oncogenic and primary immunodeficiency mutations in class IA phosphoinositide 3-Kinases. *Frontiers in Immunology* **9**:575. DOI: <https://doi.org/10.3389/fimmu.2018.00575>, PMID: 29616047
- Drew SL, Thomas-Tran R, Beatty JW, Fournier J, Lawson KV, Miles DH, Mata G, Sharif EU, Yan X, Mailyan AK, Ginn E, Chen J, Wong K, Soni D, Dhanota P, Chen PY, Shaqfeh SG, Meleza C, Pham AT, Chen A, et al. 2020. Discovery of potent and selective PI3K $\gamma$  inhibitors. *Journal of Medicinal Chemistry* **63**:11235–11257. DOI: <https://doi.org/10.1021/acs.jmedchem.0c01203>, PMID: 32865410
- Edling CE, Selvaggi F, Buus R, Maffucci T, Di Sebastiano P, Friess H, Innocenti P, Kocher HM, Falasca M. 2010. Key role of phosphoinositide 3-kinase class IB in pancreatic Cancer. *Clinical Cancer Research* **16**:4928–4937. DOI: <https://doi.org/10.1158/1078-0432.CCR-10-1210>, PMID: 20876794
- Emsley P, Lohkamp B, Scott WG, Cowtan K. 2010. Features and development of coot. *Acta Crystallographica. Section D, Biological Crystallography* **66**:486–501. DOI: <https://doi.org/10.1107/S0907444910007493>, PMID: 20383002
- Evans CA, Liu T, Lescarbeau A, Nair SJ, Grenier L, Pradeilles JA, Glenadel Q, Tibbitts T, Rowley AM, DiNitto JP, Brophy EE, O'Hearn EL, Ali JA, Winkler DG, Goldstein SI, O'Hearn P, Martin CM, Hoyt JG, Soglia JR, Cheung C, et al. 2016. Discovery of a selective Phosphoinositide-3-Kinase (PI3K)- $\gamma$  inhibitor (IPI-549) as an Immuno-Oncology clinical candidate. *ACS Medicinal Chemistry Letters* **7**:862–867. DOI: <https://doi.org/10.1021/acsmchemlett.6b00238>
- Flinn IW, Kahl BS, Leonard JP, Furman RR, Brown JR, Byrd JC, Wagner-Johnston ND, Coutre SE, Benson DM, Peterman S, Cho Y, Webb HK, Johnson DM, Yu AS, Ulrich RG, Godfrey WR, Miller LL, Spurgeon SE. 2014. Idelalisib, a selective inhibitor of phosphatidylinositol 3-kinase- $\delta$ , as therapy for previously treated indolent non-Hodgkin lymphoma. *Blood* **123**:3406–3413. DOI: <https://doi.org/10.1182/blood-2013-11-538546>, PMID: 24615776
- Fruman DA, Chiu H, Hopkins BD, Bagrodia S, Cantley LC, Abraham RT. 2017. The PI3K pathway in human disease. *Cell* **170**:605–635. DOI: <https://doi.org/10.1016/j.cell.2017.07.029>, PMID: 28802037
- Fruman DA, Rommel C. 2014. PI3K and Cancer: lessons, challenges and opportunities. *Nature Reviews Drug Discovery* **13**:140–156. DOI: <https://doi.org/10.1038/nrd4204>
- Furet P, Guagnano V, Fairhurst RA, Imbach-Weese P, Bruce I, Knapp M, Fritsch C, Blasco F, Blanz J, Aichholz R, Hamon J, Fabbro D, Caravatti G. 2013. Discovery of NVP-BYL719 a potent and selective phosphatidylinositol-3 kinase alpha inhibitor selected for clinical evaluation. *Bioorganic & Medicinal Chemistry Letters* **23**:3741–3748. DOI: <https://doi.org/10.1016/j.bmcl.2013.05.007>, PMID: 23726034
- Gangadhara G, Dahl G, Bohnacker T, Rae R, Gunnarsson J, Blaho S, Öster L, Lindmark H, Karabelas K, Pemberton N, Tyrchan C, Mogemark M, Wymann MP, Williams RL, Perry MWD, Papavoine T, Petersen J. 2019. A class of highly selective inhibitors bind to an active state of PI3K $\gamma$ . *Nature Chemical Biology* **15**:348–357. DOI: <https://doi.org/10.1038/s41589-018-0215-0>, PMID: 30718815
- Ge Y, He Z, Xiang Y, Wang D, Yang Y, Qiu J, Zhou Y. 2019. The identification of key genes in nasopharyngeal carcinoma by bioinformatics analysis of high-throughput data. *Molecular Biology Reports* **46**:2829–2840. DOI: <https://doi.org/10.1007/s11033-019-04729-3>, PMID: 30830589
- Goncalves MD, Hopkins BD, Cantley LC. 2018. Phosphatidylinositol 3-Kinase, growth disorders, and Cancer. *New England Journal of Medicine* **379**:2052–2062. DOI: <https://doi.org/10.1056/NEJMra1704560>, PMID: 30462943
- Heffron TP, Heald RA, Ndubaku C, Wei B, Augustin M, Do S, Edgar K, Eigenbrot C, Friedman L, Gancia E, Jackson PS, Jones G, Kolesnikov A, Lee LB, Lesnick JD, Lewis C, McLean N, Mörtl M, Nonomiya J, Pang J, et al. 2016. The rational design of selective benzoxazepin inhibitors of the  $\alpha$ -Isoform of phosphoinositide 3-Kinase culminating in the identification of (S)-2-((2-(1-Isopropyl-1H-1,2,4-triazol-5-yl)-5,6-dihydrobenzof[*f*]imidazo[1,2-*d*][1,4]oxazepin-9-yl)oxy)propanamide (GDC-0326). *Journal of Medicinal Chemistry* **59**:985–1002. DOI: <https://doi.org/10.1021/acs.jmedchem.5b01483>, PMID: 26741947
- Hirsch E, Katanaev VL, Garlanda C, Azzolino O, Pirota L, Silengo L, Sozzani S, Mantovani A, Altruda F, Wymann MP. 2000. Central role for G protein-coupled phosphoinositide 3-kinase gamma in inflammation. *Science* **287**:1049–1053. DOI: <https://doi.org/10.1126/science.287.5455.1049>, PMID: 10669418



- Jorgensen WL**, Chandrasekhar J, Madura JD, Impey RW, Klein ML. 1983. Comparison of simple potential functions for simulating liquid water. *The Journal of Chemical Physics* **79**:926–935. DOI: <https://doi.org/10.1063/1.445869>
- Kabsch W**. 2010. XDS. *Acta Crystallographica. Section D, Biological Crystallography* **66**:125–132. DOI: <https://doi.org/10.1107/S0907444909047337>, PMID: 20124692
- Kaneda MM**, Cappello P, Nguyen AV, Ralainirina N, Hardamon CR, Foubert P, Schmid MC, Sun P, Mose E, Bouvet M, Lowy AM, Valasek MA, Sasik R, Novelli F, Hirsch E, Varner JA. 2016a. Macrophage PI3K $\gamma$  drives pancreatic ductal adenocarcinoma progression. *Cancer Discovery* **6**:870–885. DOI: <https://doi.org/10.1158/2159-8290.CD-15-1346>, PMID: 27179037
- Kaneda MM**, Messer KS, Ralainirina N, Li H, Leem CJ, Gorjestani S, Woo G, Nguyen AV, Figueiredo CC, Foubert P, Schmid MC, Pink M, Winkler DG, Rausch M, Palombella VJ, Kutok J, McGovern K, Frazer KA, Wu X, Karin M, et al. 2016b. PI3K $\gamma$  is a molecular switch that controls immune suppression. *Nature* **539**:437–442. DOI: <https://doi.org/10.1038/nature19834>, PMID: 27642729
- Kang S**, Denley A, Vanhaesebroeck B, Vogt PK. 2006. Oncogenic transformation induced by the p110beta, -gamma, and -delta isoforms of class I phosphoinositide 3-kinase. *PNAS* **103**:1289–1294. DOI: <https://doi.org/10.1073/pnas.0510772103>, PMID: 16432180
- Knight ZA**, Gonzalez B, Feldman ME, Zunder ER, Goldenberg DD, Williams O, Loewith R, Stokoe D, Balla A, Toth B, Balla T, Weiss WA, Williams RL, Shokat KM. 2006. A pharmacological map of the PI3-K family defines a role for p110alpha in insulin signaling. *Cell* **125**:733–747. DOI: <https://doi.org/10.1016/j.cell.2006.03.035>, PMID: 16647110
- Knight SD**, Adams ND, Burgess JL, Chaudhari AM, Darcy MG, Donatelli CA, Luengo JL, Newlander KA, Parrish CA, Ridgers LH, Sarpong MA, Schmidt SJ, Van Aller GS, Carson JD, Diamond MA, Elkins PA, Gardiner CM, Garver E, Gilbert SA, Gontarek RR, et al. 2010. Discovery of GSK2126458, a highly potent inhibitor of PI3K and the mammalian target of rapamycin. *ACS Medicinal Chemistry Letters* **1**:39–43. DOI: <https://doi.org/10.1021/ml900028r>, PMID: 24900173
- Kozasa T**. 2004. Purification of G protein subunits from Sf9 insect cells using hexahistidine-tagged alpha and beta gamma subunits. *Methods in Molecular Biology* **237**:21–38. DOI: <https://doi.org/10.1385/1-59259-430-1:21>, PMID: 14501036
- Kurig B**, Shymanets A, Bohnacker T, Prajwal BC, Brock C, Ahmadian MR, Schaefer M, Gohla A, Harteneck C, Wymann MP, Jeanclous E, Nürnberg B. 2009. Ras is an indispensable coregulator of the class IB phosphoinositide 3-kinase p87/p110gamma. *PNAS* **106**:20312–20317. DOI: <https://doi.org/10.1073/pnas.0905506106>, PMID: 19906996
- Laffargue M**, Calvez R, Finan P, Trifilieff A, Barbier M, Altruda F, Hirsch E, Wymann MP. 2002. Phosphoinositide 3-kinase gamma is an essential amplifier of mast cell function. *Immunity* **16**:441–451. DOI: [https://doi.org/10.1016/S1074-7613\(02\)00282-0](https://doi.org/10.1016/S1074-7613(02)00282-0), PMID: 11911828
- Laskowski RA**, Swindells MB. 2011. LigPlot+: multiple ligand-protein interaction diagrams for drug discovery. *Journal of Chemical Information and Modeling* **51**:2778–2786. DOI: <https://doi.org/10.1021/ci200227u>, PMID: 21919503
- Li Z**, Jiang H, Xie W, Zhang Z, Smrcka AV, Wu D. 2000. Roles of PLC-beta2 and -beta3 and PI3Kgamma in chemoattractant-mediated signal transduction. *Science* **287**:1046–1049. DOI: <https://doi.org/10.1126/science.287.5455.1046>, PMID: 10669417
- Lindhurst MJ**, Parker VE, Payne F, Sapp JC, Rudge S, Harris J, Witkowski AM, Zhang Q, Groeneveld MP, Scott CE, Daly A, Huson SM, Tosi LL, Cunningham ML, Darling TN, Geer J, Gucev Z, Sutton VR, Tziotzios C, Dixon AK, et al. 2012. Mosaic overgrowth with Fibroadipose Hyperplasia is caused by somatic activating mutations in PIK3CA. *Nature Genetics* **44**:928–933. DOI: <https://doi.org/10.1038/ng.2332>, PMID: 22729222
- Lowery MA**, Bradley M, Chou JF, Capanu M, Gerst S, Harding JJ, Dika IE, Berger M, Zehir A, Ptashkin R, Wong P, Rasalan-Ho T, Yu KH, Cercek A, Morgono E, Salehi E, Valentino E, Hollywood E, O'Reilly EM, Abou-Alfa GK. 2019. Binimetinib plus gemcitabine and cisplatin phase I/II trial in patients with advanced biliary cancers. *Clinical Cancer Research* **25**:937–945. DOI: <https://doi.org/10.1158/1078-0432.CCR-18-1927>, PMID: 30563938
- Lucas CL**, Chandra A, Nejentsev S, Condliffe AM, Okkenhaug K. 2016. PI3K $\delta$  and primary immunodeficiencies. *Nature Reviews Immunology* **16**:702–714. DOI: <https://doi.org/10.1038/nri.2016.93>, PMID: 27616589
- Luo L**, Wall AA, Yeo JC, Condon ND, Norwood SJ, Schoenwaelder S, Chen KW, Jackson S, Jenkins BJ, Hartland EL, Schroder K, Collins BM, Sweet MJ, Stow JL. 2014. Rab8a interacts directly with PI3K $\gamma$  to modulate TLR4-driven PI3K and mTOR signalling. *Nature Communications* **5**:4407. DOI: <https://doi.org/10.1038/ncomms5407>, PMID: 25022365
- Luo L**, Wall AA, Tong SJ, Hung Y, Xiao Z, Tarique AA, Sly PD, Fantino E, Marzolo MP, Stow JL. 2018. TLR crosstalk activates LRP1 to recruit Rab8a and PI3K $\gamma$  for suppression of inflammatory responses. *Cell Reports* **24**:3033–3044. DOI: <https://doi.org/10.1016/j.celrep.2018.08.028>, PMID: 30208326
- Madsen RR**, Vanhaesebroeck B. 2020. Cracking the context-specific PI3K signaling code. *Science Signaling* **13**:eaay2940. DOI: <https://doi.org/10.1126/scisignal.aay2940>, PMID: 31911433
- Maier JA**, Martinez C, Kasavajhala K, Wickstrom L, Hauser KE, Simmerling C. 2015. ff14SB: improving the accuracy of protein side chain and backbone parameters from ff99SB. *Journal of Chemical Theory and Computation* **11**:3696–3713. DOI: <https://doi.org/10.1021/acs.jctc.5b00255>, PMID: 26574453
- Mandelker D**, Gabelli SB, Schmidt-Kittler O, Zhu J, Cheong I, Huang CH, Kinzler KW, Vogelstein B, Amzel LM. 2009. A frequent kinase domain mutation that changes the interaction between PI3Kalpha and the membrane. *PNAS* **106**:16996–17001. DOI: <https://doi.org/10.1073/pnas.0908444106>, PMID: 19805105

- Masson GR**, Burke JE, Ahn NG, Anand GS, Borchers C, Brier S, Bou-Assaf GM, Engen JR, Englander SW, Faber J, Garlish R, Griffin PR, Gross ML, Guttman M, Hamuro Y, Heck AJR, Houde D, Iacob RE, Jørgensen TJD, Kaltashov IA, et al. 2019. Recommendations for performing, interpreting and reporting hydrogen deuterium exchange mass spectrometry (HDX-MS) experiments. *Nature Methods* **16**:595–602. DOI: <https://doi.org/10.1038/s41592-019-0459-y>, PMID: 31249422
- McCoy AJ**, Grosse-Kunstleve RW, Adams PD, Winn MD, Storoni LC, Read RJ. 2007. Phaser crystallographic software. *Journal of Applied Crystallography* **40**:658–674. DOI: <https://doi.org/10.1107/S0021889807021206>, PMID: 19461840
- McGibbon RT**, Beauchamp KA, Harrigan MP, Klein C, Swails JM, Hernández CX, Schwantes CR, Wang LP, Lane TJ, Pande VS. 2015. MDTraj: a modern open library for the analysis of molecular dynamics trajectories. *Biophysical Journal* **109**:1528–1532. DOI: <https://doi.org/10.1016/j.bpj.2015.08.015>, PMID: 26488642
- Miao Y**, Feher VA, McCammon JA. 2015. Gaussian accelerated molecular dynamics: unconstrained enhanced sampling and free energy calculation. *Journal of Chemical Theory and Computation* **11**:3584–3595. DOI: <https://doi.org/10.1021/acs.jctc.5b00436>, PMID: 26300708
- Miller MS**, Maheshwari S, McRobb FM, Kinzler KW, Amzel LM, Vogelstein B, Gabelli SB. 2017. Identification of allosteric binding sites for PI3K $\alpha$  oncogenic mutant specific inhibitor design. *Bioorganic & Medicinal Chemistry* **25**:1481–1486. DOI: <https://doi.org/10.1016/j.bmc.2017.01.012>
- Nava Rodrigues D**, Rescigno P, Liu D, Yuan W, Carreira S, Lambros MB, Seed G, Mateo J, Riisnaes R, Mullane S, Margolis C, Miao D, Miranda S, Dolling D, Clarke M, Bertan C, Crespo M, Boysen G, Ferreira A, Sharp A, et al. 2018. Immunogenomic analyses associate immunological alterations with mismatch repair defects in prostate Cancer. *Journal of Clinical Investigation* **128**:4441–4453. DOI: <https://doi.org/10.1172/JCI121924>, PMID: 30179225
- Okkenhaug K**. 2013. Signaling by the phosphoinositide 3-kinase family in immune cells. *Annual Review of Immunology* **31**:675–704. DOI: <https://doi.org/10.1146/annurev-immunol-032712-095946>, PMID: 23330955
- Pacold ME**, Suire S, Perisic O, Lara-Gonzalez S, Davis CT, Walker EH, Hawkins PT, Stephens L, Eccleston JF, Williams RL. 2000. Crystal structure and functional analysis of ras binding to its effector phosphoinositide 3-kinase gamma. *Cell* **103**:931–944. DOI: [https://doi.org/10.1016/S0092-8674\(00\)00196-3](https://doi.org/10.1016/S0092-8674(00)00196-3), PMID: 11136978
- Pang YT**, Miao Y, Wang Y, McCammon JA. 2017. Gaussian accelerated molecular dynamics in NAMD. *Journal of Chemical Theory and Computation* **13**:9–19. DOI: <https://doi.org/10.1021/acs.jctc.6b00931>, PMID: 28034310
- Patrucco E**, Notte A, Barberis L, Selvetella G, Maffei A, Brancaccio M, Marengo S, Russo G, Azzolino O, Rybalkin SD, Silengo L, Altruda F, Wetzker R, Wymann MP, Lembo G, Hirsch E. 2004. PI3Kgamma modulates the cardiac response to chronic pressure overload by distinct kinase-dependent and -independent effects. *Cell* **118**:375–387. DOI: <https://doi.org/10.1016/j.cell.2004.07.017>, PMID: 15294162
- Perez-Riverol Y**, Csordas A, Bai J, Bernal-Llinares M, Hewapathirana S, Kundu DJ, Inuganti A, Griss J, Mayer G, Eisenacher M, Pérez E, Uszkoreit J, Pfeuffer J, Sachsenberg T, Yilmaz S, Tiwary S, Cox J, Audain E, Walzer M, Jarnuczak AF, et al. 2019. The PRIDE database and related tools and resources in 2019: improving support for quantification data. *Nucleic Acids Research* **47**:D442–D450. DOI: <https://doi.org/10.1093/nar/gky1106>, PMID: 30395289
- Perino A**, Ghigo A, Ferrero E, Morello F, Santulli G, Baillie GS, Damilano F, Dunlop AJ, Pawson C, Walser R, Levi R, Altruda F, Silengo L, Langeberg LK, Neubauer G, Heymans S, Lembo G, Wymann MP, Wetzker R, Houslay MD, et al. 2011. Integrating cardiac PIP3 and cAMP signaling through a PKA anchoring function of p110 $\gamma$ . *Molecular Cell* **42**:84–95. DOI: <https://doi.org/10.1016/j.molcel.2011.01.030>
- Safina BS**, Elliott RL, Forrest AK, Heald RA, Murray JM, Nonomiya J, Pang J, Salphati L, Seward EM, Staben ST, Ultsch M, Wei B, Yang W, Sutherlin DP. 2017. Design of selective benzoxazepin PI3K $\delta$  inhibitors through control of dihedral angles. *ACS Medicinal Chemistry Letters* **8**:936–940. DOI: <https://doi.org/10.1021/acsmchemlett.7b00170>, PMID: 28947940
- Sali A**, Blundell TL. 1993. Comparative protein modelling by satisfaction of spatial restraints. *Journal of Molecular Biology* **234**:779–815. DOI: <https://doi.org/10.1006/jmbi.1993.1626>, PMID: 8254673
- Samuels Y**, Wang Z, Bardelli A, Silliman N, Ptak J, Szabo S, Yan H, Gazdar A, Powell SM, Riggins GJ, Willson JK, Markowitz S, Kinzler KW, Vogelstein B, Velculescu VE. 2004. High frequency of mutations of the PIK3CA gene in human cancers. *Science* **304**:554. DOI: <https://doi.org/10.1126/science.1096502>, PMID: 15016963
- Sasaki T**, Irie-Sasaki J, Jones RG, Oliveira-dos-Santos AJ, Stanford WL, Bolon B, Wakeham A, Itie A, Bouchard D, Kozieradzki I, Joza N, Mak TW, Ohashi PS, Suzuki A, Penninger JM. 2000a. Function of PI3Kgamma in thymocyte development, T cell activation, and neutrophil migration. *Science* **287**:1040–1046. DOI: <https://doi.org/10.1126/science.287.5455.1040>, PMID: 10669416
- Sasaki T**, Irie-Sasaki J, Horie Y, Bachmaier K, Fata JE, Li M, Suzuki A, Bouchard D, Ho A, Redston M, Gallinger S, Khokha R, Mak TW, Hawkins PT, Stephens L, Scherer SW, Tsao M, Penninger JM. 2000b. Colorectal carcinomas in mice lacking the catalytic subunit of PI(3)Kgamma. *Nature* **406**:897–902. DOI: <https://doi.org/10.1038/35022585>, PMID: 10972292
- Schmid MC**, Avraamides CJ, Dippold HC, Franco I, Foubert P, Ellies LG, Acevedo LM, Manglicmot JR, Song X, Wrasidlo W, Blair SL, Ginsberg MH, Cheresch DA, Hirsch E, Field SJ, Varner JA. 2011. Receptor tyrosine kinases and TLR/IL1Rs unexpectedly activate myeloid cell PI3ky, a single convergent point promoting tumor inflammation and progression. *Cancer Cell* **19**:715–727. DOI: <https://doi.org/10.1016/j.ccr.2011.04.016>, PMID: 21665146
- Shu X**, Gu J, Huang M, Tannir NM, Matin SF, Karam JA, Wood CG, Wu X, Ye Y. 2018. Germline genetic variants in somatically significantly mutated genes in tumors are associated with renal cell carcinoma risk and outcome. *Carcinogenesis* **39**:752–757. DOI: <https://doi.org/10.1093/carcin/bgy021>, PMID: 29635281

- Sievers F**, Wilm A, Dineen D, Gibson TJ, Karplus K, Li W, Lopez R, McWilliam H, Remmert M, Söding J, Thompson JD, Higgins DG. 2011. Fast, scalable generation of high-quality protein multiple sequence alignments using clustal omega. *Molecular Systems Biology* **7**:539. DOI: <https://doi.org/10.1038/msb.2011.75>, PMID: 21988835
- Somoza JR**, Koditek D, Villaseñor AG, Novikov N, Wong MH, Licican A, Xing W, Lagpacan L, Wang R, Schultz BE, Papalia GA, Samuel D, Lad L, McGrath ME. 2015. Structural, biochemical, and biophysical characterization of idelalisib binding to phosphoinositide 3-Kinase  $\delta$ . *Journal of Biological Chemistry* **290**:8439–8446. DOI: <https://doi.org/10.1074/jbc.M114.634683>
- Stephens LR**, Eguinoa A, Erdjument-Bromage H, Lui M, Cooke F, Coadwell J, Smrcka AS, Thelen M, Cadwallader K, Tempst P, Hawkins PT. 1997. The G beta gamma sensitivity of a PI3K is dependent upon a tightly associated adaptor, p101. *Cell* **89**:105–114. DOI: [https://doi.org/10.1016/S0092-8674\(00\)80187-7](https://doi.org/10.1016/S0092-8674(00)80187-7), PMID: 9094719
- Stoyanov B**, Volinia S, Hanck T, Rubio I, Loubtchenkov M, Malek D, Stoyanova S, Vanhaesebroeck B, Dhand R, Nürnberg B. 1995. Cloning and characterization of a G protein-activated human phosphoinositide-3 kinase. *Science* **269**:690–693. DOI: <https://doi.org/10.1126/science.7624799>, PMID: 7624799
- Suire S**, Coadwell J, Ferguson GJ, Davidson K, Hawkins P, Stephens L. 2005. p84, a new Gbetagamma-activated regulatory subunit of the type IB phosphoinositide 3-kinase p110gamma. *Current Biology* **15**:566–570. DOI: <https://doi.org/10.1016/j.cub.2005.02.020>, PMID: 15797027
- Takeda AJ**, Maher TJ, Zhang Y, Lanahan SM, Bucklin ML, Compton SR, Tyler PM, Comrie WA, Matsuda M, Olivier KN, Pittaluga S, McElwee JJ, Long Priel DA, Kuhns DB, Williams RL, Mustillo PJ, Wymann MP, Koneti Rao V, Lucas CL. 2019. Human PI3K $\gamma$  deficiency and its microbiota-dependent mouse model reveal immunodeficiency and tissue immunopathology. *Nature Communications* **10**:4364. DOI: <https://doi.org/10.1038/s41467-019-12311-5>, PMID: 31554793
- Tate JG**, Bamford S, Jubb HC, Sondka Z, Beare DM, Bindal N, Boutselakis H, Cole CG, Creatore C, Dawson E, Fish P, Harsha B, Hathaway C, Jupe SC, Kok CY, Noble K, Ponting L, Ramshaw CC, Rye CE, Speedy HE, et al. 2019. COSMIC: the catalogue of somatic mutations in Cancer. *Nucleic Acids Research* **47**:D941–D947. DOI: <https://doi.org/10.1093/nar/gky1015>, PMID: 30371878
- Thian M**, Hoeger B, Kamnev A, Poyer F, Köstel Bal S, Caldera M, Jiménez-Heredia R, Huemer J, Pickl WF, Groß M, Ehl S, Lucas CL, Menche J, Hutter C, Attarbaschi A, Dupré L, Boztug K. 2020. Germline biallelic PIK3CG mutations in a multifaceted immunodeficiency with immune dysregulation. *Haematologica* **105**:e488. DOI: <https://doi.org/10.3324/haematol.2019.231399>, PMID: 33054089
- Thomas M**, Edwards MJ, Sawicka E, Duggan N, Hirsch E, Wymann MP, Owen C, Trifilieff A, Walker C, Westwick J, Finan P. 2009. Essential role of phosphoinositide 3-kinase gamma in eosinophil chemotaxis within acute pulmonary inflammation. *Immunology* **126**:413–422. DOI: <https://doi.org/10.1111/j.1365-2567.2008.02908.x>, PMID: 18754810
- Torres C**, Mancinelli G, Cordoba-Chacon J, Viswakarma N, Castellanos K, Grimaldo S, Kumar S, Principe D, Dorman MJ, McKinney R, Hirsch E, Dawson D, Munshi HG, Rana A, Grippo PJ. 2019. p110 $\gamma$  deficiency protects against pancreatic carcinogenesis yet predisposes to diet-induced hepatotoxicity. *PNAS* **116**:14724–14733. DOI: <https://doi.org/10.1073/pnas.1813012116>, PMID: 31266893
- Vadas O**, Burke JE, Zhang X, Berndt A, Williams RL. 2011. Structural basis for activation and inhibition of class I phosphoinositide 3-Kinases. *Science Signaling* **4**:1–13. DOI: <https://doi.org/10.1126/scisignal.2002165>
- Vadas O**, Dbouk HA, Shymanets A, Perisic O, Burke JE, Abi Saab WF, Khalil BD, Harteneck C, Bresnick AR, Nürnberg B, Backer JM, Williams RL. 2013. Molecular determinants of PI3K $\gamma$ -mediated activation downstream of G-protein-coupled receptors (GPCRs). *PNAS* **110**:18862–18867. DOI: <https://doi.org/10.1073/pnas.1304801110>, PMID: 24190998
- Vadas O**, Jenkins ML, Dornan GL, Burke JE. 2017. Using Hydrogen-Deuterium exchange mass spectrometry to examine Protein-Membrane interactions. *Meth Enzymol* **583**:143–172. DOI: <https://doi.org/10.1016/bs.mie.2016.09.008>
- Vasan N**, Razavi P, Johnson JL, Shao H, Shah H, Antoine A, Ladewig E, Gorelick A, Lin TY, Toska E, Xu G, Kazmi A, Chang MT, Taylor BS, Dickler MN, Jhaveri K, Chandarlapaty S, Rabadan R, Reznik E, Smith ML, et al. 2019. Double PIK3CA mutations in Cis increase oncogenicity and sensitivity to PI3K $\alpha$  inhibitors. *Science* **366**:714–723. DOI: <https://doi.org/10.1126/science.aaw9032>, PMID: 31699932
- Venkatesan AM**, Dehnhardt CM, Delos Santos E, Chen Z, Dos Santos O, Ayril-Kaloustian S, Khafizova G, Brooijmans N, Mallon R, Hollander I, Feldberg L, Lucas J, Yu K, Gibbons J, Abraham RT, Chaudhary I, Mansour TS. 2010. Bis(morpholino-1,3,5-triazine) derivatives: potent adenosine 5'-triphosphate competitive phosphatidylinositol-3-kinase/mammalian target of rapamycin inhibitors: discovery of compound 26 (PKI-587), a highly efficacious dual inhibitor. *Journal of Medicinal Chemistry* **53**:2636–2645. DOI: <https://doi.org/10.1021/jm901830p>, PMID: 20166697
- Walker EH**, Perisic O, Ried C, Stephens L, Williams RL. 1999. Structural insights into phosphoinositide 3-kinase catalysis and signalling. *Nature* **402**:313–320. DOI: <https://doi.org/10.1038/46319>, PMID: 10580505
- Walser R**, Burke JE, Gogvadze E, Bohnacker T, Zhang X, Hess D, Küenzi P, Leitges M, Hirsch E, Williams RL, Laffargue M, Wymann MP. 2013. Pkc $\beta$  phosphorylates PI3K $\gamma$  to activate it and release it from GPCR control. *PLOS Biology* **11**:e1001587. DOI: <https://doi.org/10.1371/journal.pbio.1001587>, PMID: 23824069
- Wang J**, Li M, Han X, Wang H, Wang X, Ma G, Xia T, Wang S. 2020. MiR-1976 knockdown promotes epithelial-mesenchymal transition and cancer stem cell properties inducing triple-negative breast cancer metastasis. *Cell Death & Disease* **11**:500–512. DOI: <https://doi.org/10.1038/s41419-020-2711-x>

- Zhang X**, Vadas O, Perisic O, Anderson KE, Clark J, Hawkins PT, Stephens LR, Williams RL. 2011. Structure of lipid kinase p110 $\beta$ /p85 $\beta$  elucidates an unusual SH2-domain-mediated inhibitory mechanism. *Molecular Cell* **41**: 567–578. DOI: <https://doi.org/10.1016/j.molcel.2011.01.026>, PMID: 21362552
- Zhang P**, Kang B, Xie G, Li S, Gu Y, Shen Y, Zhao X, Ma Y, Li F, Si J, Wang J, Chen J, Yang H, Xu X, Yang Y. 2019. Genomic sequencing and editing revealed the GRM8 signaling pathway as potential therapeutic targets of squamous cell lung Cancer. *Cancer Letters* **442**:53–67. DOI: <https://doi.org/10.1016/j.canlet.2018.10.035>, PMID: 30391781